UNIVERSITY OF SOUTHAMPTON

FACULTY OF ENGINEERING, SCIENCE AND MATHEMATICS

School of Physics and Astronomy

Application of Planar Chirality to Nanophotonics, Astronomy and Image Analysis

by

Alexander Sven Schwanecke

Thesis for the degree of Master of Philosophy

September 2004

UNIVERSITY OF SOUTHAMPTON

ABSTRACT

FACULTY OF ENGINEERING, SCIENCE AND MATHEMATICS
SCHOOL OF PHYSICS AND ASTRONOMY

Master of Philosophy

APPLICATION OF PLANAR CHIRALITY TO NANOPHOTONICS, ASTRONOMY AND IMAGE ANALYSIS

by Alexander Sven Schwanecke

The concept of geometrical chirality has been improved introducing a unit of planar chirality and dedicated normalisation factors which facilitate the analysis of various complex chiral objects. On the basis of these improvements a highly efficient Monte Carlo computer algorithm for calculation of the planar chirality measure has been developed.

I have investigated the planar chirality of characteristic planar chiral objects such as triangles, gammadions and round gammadions and established the configurations for various parameter fields for which their chirality is maximised.

For the first time I have explored the aggregated chirality of ensembles of 2, 3 and more planar chiral structures including their regular grids. The chirality of ensembles is found to be a strong function of the mutual positions of the individual elements to an extent that the ensemble chirality can change its sign. It has furthermore been established that the chirality of regular square grids may be nonzero when constituting of achiral objects.

For the first time I have investigated the chirality and rotational and mirror symmetries of diffraction field patterns and microscopic images created by different enantiomeric forms of various planar chiral structures. I have established that the chirality of the diffraction patterns is inherited from the chiral object itself while the rotational symmetries are lower than in the underlying design.

For the first time a geometrical chirality measure has been applied to quantify the geometry of star distributions in 113 nearby galaxies. A quantitative parameter has been suggested for classification of galaxies which is based on the chirality measure.

Contents

List of Tables

List of Figures

DECLARATION OF AUTHORSHIP

I, Alexander Sven Schwanecke, declare that the thesis *Application of Planar Chirality to Nanophotonics, Astronomy and Image Analysis* and the work presented in it are my own. I confirm that:

- this work was done wholly or mainly while in candidature for a research degree at this University;
- where any part of this thesis has previously been submitted for a degree or any other qualification at this University or any other institution, this has been clearly stated;
- where I have consulted the published work of others, this is always clearly attributed;
- where I have quoted from the work of others, the source is always given. With the exception of such quotations, this thesis is entirely my own work;
- I have acknowledged all main sources of help;
- where the thesis is based on work done by myself jointly with others, I have made clear exactly what was done by others and what I have contributed myself;
- part of this work has been published as:
  A. S. Schwanecke at al. Broken time reversal of light interaction with planar chiral nanostructures. *Phys. Rev. Lett.* **91**, 247404 (2003).
  N. I. Zheludev et al. Broken time-reversal and electromagnetic anyon quasi-particles in 2D chiral plasmon structures. *Proc. Progress in Electromagnetic Research Symposium (PIERS) 2004* / Pisa, 562 (2004).
  N. I. Zheludev et al. Broken time-reversal and electromagnetic anyon quasiparticles in 2D chiral plasmon nanostructures. *Conference on Laser Electro-Optics / Internatianal Quantum Electronics Conference (CLEO / IQEC)*, CD code: IThB4 (2004).
  A. Papakostas et al. Asymmetric diffraction from regular, quasi-random and fractal planar chiral nano-structures. *Conference on Quantum Electronics and Photonics QEP-16* at Photon04 (IoP), abstract reference 000060 (2004).

Signature [redacted] Date 30 Sep 2004

Acknowledgements

I would like to thank my supervisor, Professor Nikolay Zheludev, for the opportunity to pursue this research and his constant feedback, ideas, help and contributions which were invaluable for the success of this work.

Also, I would like to thank the members of the Nanophotonics Group for the many fruitful discussions and their help on the smaller and bigger problems that I faced. Particularly I would like to mention Mr. Aris Papakostas with whom I also collaborated on the diffraction experiments discussed in Sec. 3.1. I am furthermore grateful for the fruitful discussions with Mr. Alexey Krasavin and Dr. Vassili Fedotov on the topics of planar chirality and time non-reversal.

Much of the experimental work would not have been possible without Dr. Darren Bagnall and Dr. Adrian Potts and their fabrication of the nanostructured samples discussed in the last chapter.

I would like to acknowledge helpful discussions with Dr. Adrian Potts about planar chirality. I am also grateful to Professor Sergey Prosvirnin who helped in discussions on his visits with his inspiration and his perspective of chirality towards physics and non-reciprocity.

Furthermore I would like to thank Dr. Anatoly Zayats who's feedback and contributions on the issues of time non-reversal were crucial.

Last but not least I would like to acknowledge the generous support of the German National Academic Foundation (Studienstiftung des deutschen Volkes) and the Engineering and Physical Sciences Research Council (UK).

Southampton, UK
September, 2004

Alexander Sven Schwanecke

Definitions and Abbreviations

Abbreviations

DP	diffraction pattern
PCS	planar chiral structure

Definitions

$\mathbb{N} = \{0, 1, 2, 3, \ldots\}$	set of natural numbers (including zero);
$\mathbb{Z} = \{\ldots, -2, -1, 0, 1, 2, \ldots\}$	set of integer numbers.

Other

The bibliography contains the document object identifier (DOI) for many articles. In order to retrieve these articles online append the code to the URL `http://dx.doi.org/`.

1 Introduction

The advances in micro- and nano-fabrication of the last decade open a completely new chapter of photonics. A whole new approach in regard to light matter interactions has been made available. The, nowadays also commercial, availability of production facilities for near arbitrarily structured devices of dimensions much smaller than the wavelengths of the visible spectrum of light allows to design specific material properties. Amongst the possibilities are **meta-materials** with e.g. negative refractivity, a property which has not before been found in nature.

The last years have brought numerous articles on topics like photonic crystals and quantum dots and wires focussing on three-dimensional structures or fields where the interaction processes are dominated by quantum effects. In between lies an area which promises to create miniaturized optical devices with broadly tunable features, like nano-mirrors or polarisation converters [Hooper and Sambles, 2002]. The concept of 3D optical activity has long been known in nature and found many applications in the various natural sciences. Fabrication techniques, similar to those used for the creation of chips, allow planar structures with characteristics resembling the 3D optical activity and its rotation of the polarisation azimuth of light. These planar structures have a special symmetry property called **chirality** which is responsible for their behaviour [Papakostas et al., 2003].

The work by Potts et al. [2004] has resulted into the development of a novel measure of this **planar chirality** which enables to distinguish to which level an object exhibits chirality. Its simplicity and scalability equip it with strengths that have not been seen in that combination for earlier suggestions of possible chirality measures. First results allowing to suspect a relation between this geometrical property and the polarisation azimuth rotation for light mat-

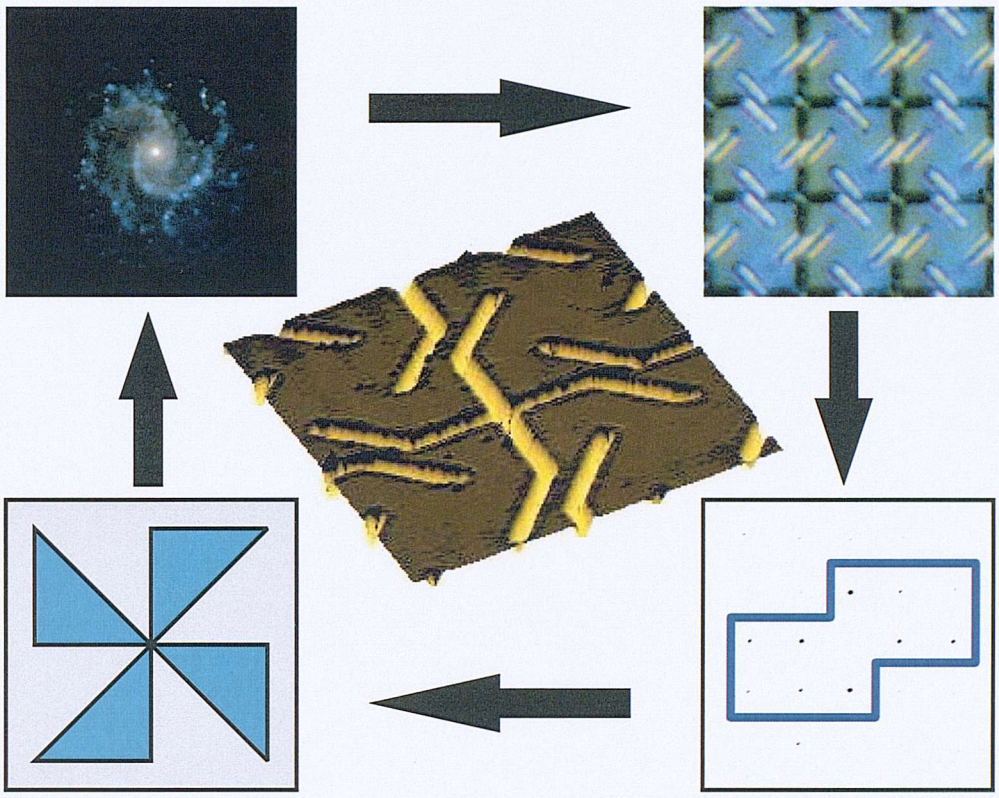

Figure 1.1: Several examples of planar chiral structures.

ter interactions with planar chiral nanostructures have encouraged a thorough examination of planar chirality and its prospects for photonics.

This thesis reviews the idea of the planar chirality measure and discusses properties and refinements which have not previously been noted. Most notably is the development and discovery of a possible unit for this planar chirality which follows directly from the concept of the measure.

In practical situations the complexity of problems might make the direct calculation of the measure impossible within sensible time scales. An approach to by-pass this limitation using the Monte Carlo technique is developed and discussed in detail. This work has resulted in a programme suite able to provide chirality measures for a variety of problems and applications.

Its capabilities are tested for increasing complexity of various planar chiral

designs. These results are particularly intended to complement experimental and numerical results gained by other members of the author's group and its collaborators. Among the main conclusions is the applicability of nearest-neighbour considerations for large grids of a single chiral object type.

Experiments performed on planar chiral nanostructures (PCS) round up the picture. It has been found that specific structures display time non-reversal interactions which appear to stem from the particular chiral design. This observation would constitute the first observation of a time non-reversal interaction in nonmagnetic media. Furthermore various peculiarities of the symmetries of diffraction patterns of PCS are discussed and linked with the term chirality.

Finally the planar chirality measure will be applied to the discipline of galaxy morphology. Here the Monte Carlo technique proves its strengths and a general suggestion to astronomers to consider the measure to judge the spirality of galaxies is made. The successful feasibility study results into the availability of an analysed catalogue of 113 galaxies ready for inspection by astronomers.

1.1 Chirality

The word **chiral** stems from the Greek word for hand which is the simplest example of a chiral object as there exist left and right version (or enantiomers) of it. The definition used nowadays goes back to Lord Kelvin and the beginning of the last century [Kelvin, 1904]:

> I call any geometrical figure (...) chiral, and say it has chirality, if its image in a plane mirror (...) cannot be brought to coincide with itself.[1]

An intuitive way to communicate what this means can be followed on every table: Put your hands on the table next to one another with your palms laying on the table top. You will see that your hands (at least in a rough estimation) are mirror images of another existing as planar objects on the table top. If you try to translate and rotate your hands in this plane, you will see that their shapes can never fully coincide. Only lifting one of your hands out of this

[1] Citation taken from Le Guennec [2000].

plane and letting the back of this hand face the table allows their complete coincidence: Your hands are chiral in the truest sense of the word and you may disentangle them now.

Two objects which are mirror images of one another are called **enantiomers**. The terminology around chirality has largely been coined by the chemistry community, where various applications of this concept exist on a mostly molecular level. It stems from the discovery that objects consisting of the same elements in a mirror image configuration can have significantly different chemical properties. An introduction into the relations of chemistry and chirality has e.g. been given by the Nobel laureate Prelog [1976]. Recent publications report of the various molecular processes which rely on chirality, including areas like enzyme catalysis which opens the connection to biochemistry [de Jong et al., 2004].

In biology the concept of chirality allows e.g. to distinguish bacteria which share a mirror-symmetric buildup, but differ considerably property-wise. These terms have recently even reached public television as advertisement campaigns refer to them. Lactic acid e.g. exists in two enantiomeric forms denoted D(−) and L(+) where latter can much better be broken down by the body and its favoured consumption is suggested by health professionals.

However all these terms have their roots in the concept of optical activity. In 1846 Faraday discovered the rotation of the polarisation plane of linear polarised light when applying a magnetic field. Two years later Pasteur noted the opposite but equal amount of polarisation azimuth rotation by different crystals of sodium ammonium tartrate. Finally it took until Lord Kelvin to understand the difference between magnetic rotation and natural optical activity and to introduce the term chirality to describe latter phenomenon [Barron, 2000].

Its mathematically developed concept has stimulated research in various areas. It is frequently cited in work on bi-anisotropic media where 3D chiral objects like e.g. spirals are investigated [Semchenko et al., 1998]. Also various configurations of the in recent years much favoured carbon nanotubes are chiral.

The theory of classical electromagnetism still develops to integrate and discuss interactions with chiral structures, so e.g. the development of the chiral

Maxwell-Garnett mixing formula [Shivola and Lindell, 1990]. Other approaches particularly by the microwave community use pseudo-chiral materials, e.g. the so called Ω-materials, to artificially create the coupling of electric and magnetic fields known for chiral materials [Saadoun and Engheta, 1992].

The development of meta-materials has reached a recent climax with the discovery of artificial materials with negative refractive index [Pendry, 2000, 2003; Pendry and Ramakrishna, 2003].

Following several theoretical considerations like those by Hecht and Barron [1994], Viitanen and Puska [1997] and Zouhdi et al. [1999] last year two publications reported of experimental results on planar chiral nanostructures: Papakostas et al. [2003] and later Vallius et al. [2003] have demonstrated the importance of the concept of planar chirality for nanostructured optical devices and triggered a number of further publications [Potts et al., 2004, 2003; Prosvirnin and Zheludev, 2003; Schwanecke et al., 2003; Wright and Zheludev, 2003].

1.2 Planar chirality measure

The development of chirality measures has occupied various research groups [Harris et al., 1999; Le Guennec, 2000; Petitjean, 2003; Zabrodsky and Avnir, 1995] and often resulted into the need for optimisation techniques to actually calculate chirality [Buda et al., 1992; Buda and Mislow, 1992; Petitjean, 1999, 2002]. Many of these measures use quite complicated approaches and calculate minimum distances or overlap areas of single objects with their enantiomers.

The obvious disadvantage are difficulties for large or infinite structures and early limitations for complex structures. An intriguingly different approach has been started by Osipov et al. [1998]. The physically motivated construction brought the concept of describing an object as a superposition of 3-point triangles with it. The geometrically simplest chiral configuration is a set of three points and the simplicity of this approach results into its potency.

Latter approach was in the end formulated using physical considerations instead of purely mathematical or geometrical ones. Potts et al. [2004] took on this next step and while using the underlying concept of Osipov et al. [1998]

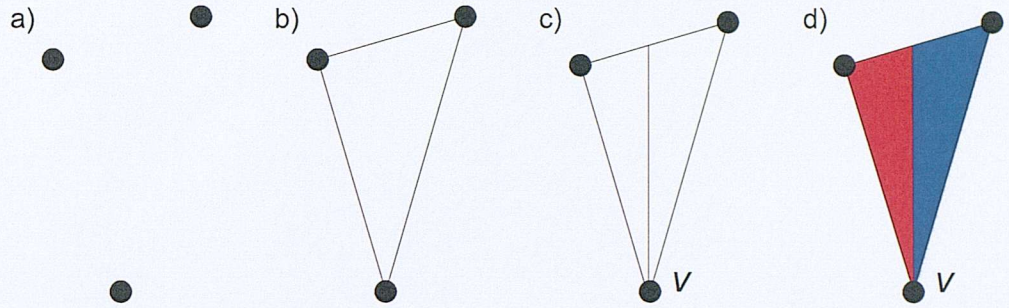

Figure 1.2: Potts et al. [2004] describe the chirality of a set of three points (a) using the triangle area they define (b). Seen from vertex V the area is divided by angular bisection (c). The relative difference of the resulting areas in relation to the overall area of the triangle is the chiral contribution of vertex V (d).

redefined the measure to be purely geometrical. This measure finds numerous applications and is the main focus of this thesis. Its idea again is to consider a single three-point triangle and to associate a certain chirality with it summing up the results for all vertices to represent the complete triangle.

The chirality seen by a single vertex uses angular bisection to divide the overall triangle area into two parts. The relative difference between the areas to the left and right of the bisection is associated with the chirality, see Fig. 1.2. An alternative, simpler definition will be introduced in chapter 2. In further steps and using a set of postulates a multiplication with the overall area of the triangle and masses in the vertices concludes the calculation:

The measure of planar chirality is defined by summing over all possible triangle combinations of a discretised object with their vertices being at $\boldsymbol{r}_i, \boldsymbol{r}_j, \boldsymbol{r}_k$ within the x, y-plane and corresponding masses of m_i, m_j, m_k as [Potts et al., 2004, Eq. (17)]:

$$K = \frac{1}{4} \sum_{i=1}^{N} \sum_{j=1}^{N} \sum_{k=1}^{N} m_i m_j m_k \frac{|\boldsymbol{r}_{ij}| - |\boldsymbol{r}_{ik}|}{|\boldsymbol{r}_{ij}| + |\boldsymbol{r}_{ik}|} (\boldsymbol{r}_{ij} \times \boldsymbol{r}_{ik}) \tag{1.1}$$

where $\boldsymbol{r}_{ij} = \boldsymbol{r}_j - \boldsymbol{r}_i$, $\boldsymbol{r}_{ik} = \boldsymbol{r}_k - \boldsymbol{r}_i$.

The continuous equivalent of an object described by its density function $\rho(\boldsymbol{r})$

is [Potts et al., 2004, Eq. (18)]:

$$K = \frac{1}{4} \int_{\boldsymbol{r}_i} \int_{\boldsymbol{r}_j} \int_{\boldsymbol{r}_k} \rho(\boldsymbol{r}_i)\rho(\boldsymbol{r}_j)\rho(\boldsymbol{r}_k) \frac{|\boldsymbol{r}_{ij}| - |\boldsymbol{r}_{ik}|}{|\boldsymbol{r}_{ij}| + |\boldsymbol{r}_{ik}|} (\boldsymbol{r}_{ij} \times \boldsymbol{r}_{ik}) \, \mathrm{d}^2\boldsymbol{r}_i \, \mathrm{d}^2\boldsymbol{r}_j \, \mathrm{d}^2\boldsymbol{r}_k \quad (1.2)$$

The following chapter will discuss these equations in detail.

2 Investigation of Planar Chirality

The concept of a novel measure of planar chirality developed by Potts et al. [2004] demands a thorough investigation under the light of its numerous possible applications. The first part of this chapter is dedicated to point out its various properties, redefine parts of it to aid consistency and introduce novel additional concepts like a unit of chirality.

The measure introduces some difficulty for the calculation of large and complex objects as its amount of necessary calculations scales cubically with the number of involved masses or objects. It will be shown that the Monte Carlo technique allows to consider a considerably increased amount of structures. A programme suite using the developed algorithm has been established to tackle the various numerical calculational needs that arise for the running projects on planar chirality.

At the example of structures, which are not only abstract but also exist as nanostructured samples, the trail of chirality for developing complexity will be followed. Apart from data to be used to compare with past and future experimental results, techniques to describe the chirality of large arrays will be described.

2.1 General considerations

The chirality measure proposed by Potts et al. [2004], see Eq. (1.1) and (1.2), has been compared in great detail to other measures and successfully applied to create a link to polarisation azimuth rotation of light by planar chiral nanostructures [Papakostas et al., 2003]. Yet there are still various matters concerning the significance of the involved parameters and their way of implementation to be considered—particularly in relation to application and the measuring pro-

cess itself. The following sections will be dedicated to this discussion and offer new suggestions as well as an improved understanding.

2.1.1 Definition

The planar chirality index or measure[1] has originally been motivated by a relative comparison of the areas when dividing a triangle by angular bisection. This introduction of the measure is consistent with the discussion of the other examples of possible triangle divisions and the comparison of the involved areas within the article by Potts et al. [2004]. However it can be introduced even more straightforward: Instead of suggesting the complex derivation of the sectioned areas, it might be motivated as the differences of the triangle sides attached to each vertex divided by their individual sum. This allows considerably quicker perception and understanding of the concept both graphically and algebraically while ensuring equivalence to the original concept.

In anticipation of the upcoming considerations it will be helpful to introduce a revised definition of the chirality measure already incorporating all of the to be suggested changes at this stage. While the general idea is not changed, the refinements provide some significant advantages. For a discrete planar distribution (e.g. within the x, y-plane) each of the triangle combinations with the vertices $\boldsymbol{r}_i, \boldsymbol{r}_j, \boldsymbol{r}_k$ (in N different coordinates) and their masses m_i, m_j, m_k will be considered as part of

$$\kappa = \frac{1}{12} \sum_{i=1}^{N} \sum_{j=1}^{N} \sum_{k=1}^{N} m_i m_j m_k \left(\frac{|\boldsymbol{r}_{ij}| - |\boldsymbol{r}_{ik}|}{|\boldsymbol{r}_{ij}| + |\boldsymbol{r}_{ik}|} + \frac{|\boldsymbol{r}_{jk}| - |\boldsymbol{r}_{ji}|}{|\boldsymbol{r}_{jk}| + |\boldsymbol{r}_{ji}|} + \frac{|\boldsymbol{r}_{ki}| - |\boldsymbol{r}_{kj}|}{|\boldsymbol{r}_{ki}| + |\boldsymbol{r}_{kj}|} \right) \times (\boldsymbol{r}_{ij} \times \boldsymbol{r}_{ik}) \cdot \widehat{\boldsymbol{e}}_{\text{obs}} \,, \tag{2.1}$$

where $\boldsymbol{r}_{\alpha\beta} = \boldsymbol{r}_\beta - \boldsymbol{r}_\alpha$ with $\alpha, \beta \in \{i, j, k\}$ are side lengths of the triangles and $\widehat{\boldsymbol{e}}_{\text{obs}}$ is a normal vector directed at the observer. Latter for the common case of the object in the x, y-plane will equal $\widehat{\boldsymbol{e}}_z$, the normal vector in $+z$-direction.

A continuous mass distribution on the other hand, given by its density func-

[1] It will be referred to solely as chirality where the context is unambiguous.

tion $\rho(\boldsymbol{r})$, can be evaluated using the expression:

$$\kappa = \frac{1}{12}\int_{r_i}\int_{r_j}\int_{r_k}\rho(\boldsymbol{r}_i)\rho(\boldsymbol{r}_j)\rho(\boldsymbol{r}_k)\left(\frac{|\boldsymbol{r}_{ij}|-|\boldsymbol{r}_{ik}|}{|\boldsymbol{r}_{ij}|+|\boldsymbol{r}_{ik}|}+\frac{|\boldsymbol{r}_{jk}|-|\boldsymbol{r}_{ji}|}{|\boldsymbol{r}_{jk}|+|\boldsymbol{r}_{ji}|}+\frac{|\boldsymbol{r}_{ki}|-|\boldsymbol{r}_{kj}|}{|\boldsymbol{r}_{ki}|+|\boldsymbol{r}_{kj}|}\right) \times (\boldsymbol{r}_{ij}\times\boldsymbol{r}_{ik})\cdot\widehat{\boldsymbol{e}}_{\text{obs}}\,\mathrm{d}^2\boldsymbol{r}_i\,\mathrm{d}^2\boldsymbol{r}_j\,\mathrm{d}^2\boldsymbol{r}_k \tag{2.2}$$

using the same shorthands as before. As this section aims to provide for the introduction of the Monte Carlo approximation of the chirality measure, only the discrete version will be discussed. Still most considerations have their continuous analogon.

The introduced visit of every vertex every single time a triangle combination is considered, is particularly time-saving for approximation methods like the Monte Carlo method, as less random numbers have to be generated. Because every triangle will be evaluated $6 = 1!\cdot 2!\cdot 3!$ times and the cross-product results in twice the triangle area, the overall equation has been scaled by a factor of 12.

For direct, non-approximative calculations of the chirality measure these repeated visits can of course be omitted. The discrete version, Eq. (2.1), can equivalently be rewritten employing the constraint $i < j < k$ as:

$$\kappa = \frac{1}{2}\sum_{i=1}^{N}\sum_{j=1+i}^{N}\sum_{k=1+j}^{N} m_i m_j m_k\left(\frac{|\boldsymbol{r}_{ij}|-|\boldsymbol{r}_{ik}|}{|\boldsymbol{r}_{ij}|+|\boldsymbol{r}_{ik}|}+\frac{|\boldsymbol{r}_{jk}|-|\boldsymbol{r}_{ji}|}{|\boldsymbol{r}_{jk}|+|\boldsymbol{r}_{ji}|}+\frac{|\boldsymbol{r}_{ki}|-|\boldsymbol{r}_{kj}|}{|\boldsymbol{r}_{ki}|+|\boldsymbol{r}_{kj}|}\right) \times (\boldsymbol{r}_{ij}\times\boldsymbol{r}_{ik})\cdot\widehat{\boldsymbol{e}}_{\text{obs}}\,. \tag{2.3}$$

2.1.2 Interpretation of the area normal

The original article [Potts et al., 2004] demands a single valued chirality measure. Yet their definition results into a vector which of course can be well motivated in relation to the term twist and its description by polar vectors. However chirality normally is referred to as a pseudoscalar. If the planar object is not located within one of the planes defined by the axes of the coordinate system, it will become more difficult to discuss, matters like sign changes and other properties. Introducing the scalar product with a normal vector $\widehat{\boldsymbol{e}}_{\text{obs}}$ creates a scalar chirality measure and generalises the validity for variations of

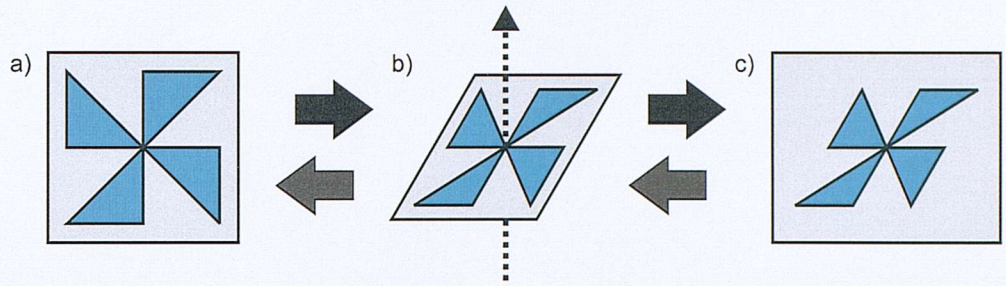

Figure 2.1: If a planar chiral structure (a) is observed at an angle (b), its virtual planar image (c) will be deformed and its therefore virtual chirality will be different to the one measured within the plane of the original object. Using the refined definition of the chirality index the influence of the observation direction can be approximated.

coordinate systems. For the cases discussed within this chapter the objects are always considered to exist within the x, y-plane defining $\widehat{e}_{\text{obs}} = \widehat{e}_z$.

Furthermore will the influence of a planar chiral object be changed if observed at an angle. Depending on the case it might be advisable to project the object on a plane perpendicular to the observation direct and create a new set of coordinates $\boldsymbol{r}$ and masses m. For small tilts or where internal processes within the PCS dominate, instead $\widehat{e}_{\text{obs}}$ might just be seen as opposing the observation direction. It there describes the influence of the relative area proportionality of the chirality measure.

For an example situation, where these re-normalisations of the measure are applicable, see Sec. 3.3. Using this understanding of the area normal it might also be possible to measure 3D chirality defined by a set of 4 points forming pyramid like structures. The triangular faces of these tetrahedrons are associated with their chirality vectors and can be summed up. This could be an extension of the planar theory to 3D space, but has to part of another investigation.

2.1.3 Area–dependence

The cross-product embedded in κ results into a direct proportionality to the area of an object. However in a truely mathematical sense, an object with the

same symmetry exhibits the same level of chirality regardless of its scale. It is therefore appropriate to define a separate *area-normalised* chirality measure

$$\kappa_a = \frac{1}{A}\kappa\,, \tag{2.4}$$

where A is exactly or representative for the area occupied by the mass distribution.

If accepting the area influence, this division also allows another interpretation in relation to κ: It represents the chirality in relation to how close a chiral mass distribution can be arranged with other objects. This is particularly interesting with regard to the arrangement of e.g. gammadion structures in arrays, see Sec. 2.3.3.

2.1.4 Mass–dependence

The measure κ is also proportional to the cube of the involved masses. Potts et al. [2004] give an explanation with regard to the possibility of splitting a mass in two or more, which e.g. would be the case for an increased resolution of a discretisation. Yet it creates an artificial and pronounced sensitivity to small changes within the overall mass of an object that can easily dominate structural hence symmetry affecting property changes. This particularly is the case for the discretisations of objects which will be discussed in Sec. 2.3 and stimulates the definition of a *mass-normalised* chirality measure

$$\kappa_m = \left(\sum_{i=1}^{N} m_i\right)^{-3} \kappa \tag{2.5}$$

and, together with the considerations of the previous section, a *fully* or *area- and mass-normalised* chirality measure

$$\kappa_{am} = \frac{1}{A}\left(\sum_{i=1}^{N} m_i\right)^{-3} \kappa \tag{2.6}$$

The independence of the involved masses is also legitimate, because the chi-

rality measure is purely geometrical: It cannot detect chirality which stems from an unequal distribution of mass between the vertices. An equilateral triangle e.g. with different masses in all vertices is chiral per definition, because its enantiomer cannot be superimposed with it without lifting it out of the plane.

The same consideration is true for isosceles triangles. Various attempts to unify geometrical and mass chirality have shown that a chirality respecting both influences cannot be single valued: All single valued approaches produce conditions under which any scalene triangle can have zero chirality if the relative, but nonzero masses of the vertices are chosen accordingly.

2.1.5 A unit of chirality

One of the most exciting prospects of this measure of chirality is the possibility to introduce a unit. The underlying theory is based on the concept of triangle superposition, hence a master object for its unit should be a triangle or set of 3 points respectively. Investigation reveals that a maximum chiral triangle shape exists. It can easily be determined setting just a few constraints to fix its scale:

A set of 3 points with equal masses of 1 defines a triangle with the side lengths a, b, c (named counterclockwise), where initially $c > a > b$ and $c = 1$ are chosen to force a unique solution. The area of the triangle A is given by [Bronstein et al., 2000]

$$A_\Delta = \sqrt{\left(\frac{a+b+c}{2} - a\right)\left(\frac{a+b+c}{2} - b\right)\left(\frac{a+b+c}{2} - c\right)\left(\frac{a+b+c}{2}\right)} \tag{2.7}$$

and its chirality can be evaluated with reference to Eq. (2.1) as

$$\kappa_\Delta = \left(\frac{c-a}{c+a} + \frac{a-b}{a+b} + \frac{b-c}{b+c}\right) \cdot A_\Delta \,. \tag{2.8}$$

Necessary conditions for an extremum applying above constraints and statements are

$$\left.\frac{\partial \kappa_\Delta}{\partial a}\right|_{c=1} = 0 \quad \text{and} \quad \left.\frac{\partial \kappa_\Delta}{\partial b}\right|_{c=1} = 0 \,. \tag{2.9}$$

The joint solution of these partial differential equations is not trivial, but can easily be approximated using e.g. Matlab[2]: The results are shown in Tab. 2.1. However most of the obtained solutions are complex or contain negative values and therefore have to be excluded. The solution $a = b = c = 1$ naturally has zero chirality and is saddle point alike. The remaining two solutions are sorted out farther by considering the constraint $c > a > b$, so that only the solution

$$\begin{aligned} a_{\max} &= 0.789914351519603\ldots \\ b_{\max} &= 0.322757101679095\ldots \\ c_{\max} &= 1 \end{aligned} \tag{2.10}$$

remains where

$$\left.\frac{\partial^2 \kappa_\Delta}{\partial a^2} \cdot \frac{\partial^2 \kappa_\Delta}{\partial b^2} - \left(\frac{\partial^2 \kappa_\Delta}{\partial a\, \partial b}\right)^2 \right|_{a_{\max}, b_{\max}, c_{\max}} \leq 0 \tag{2.11}$$

confirms the detection of a maximum.

The area of this triangle is $A_{\max} = 0.1078$. Combined with the initial assumption that all three points have masses of 1, the flexibility of this solution is challenged in view of area- and mass-normalisation. When employing the additional constraints $A = 1$ and $\sum_{i=1}^{3} m_i = 1$ while abandoning $c = 1$ one is left with a scaled and less weighty version of the upper triangle solution:

$$\begin{aligned} a_{\max,\mathrm{n}} &= 2.40535733702210\ldots \\ b_{\max,\mathrm{n}} &= 0.982823215081864\ldots \\ c_{\max,\mathrm{n}} &= 3.04508625826937\ldots \end{aligned} \tag{2.12}$$

which for a fixed length of c still represents a maximum chiral triangle. This one however is outstanding, because it is fully standardized with a chirality of

$$\hat{\kappa} \approx 9.34460344766886 \cdot 10^{-4}. \tag{2.13}$$

[2]For details see: `http://www.mathworks.com/`

Side a	Side b
1	1
1.7502+0.79880*i	-1.4100-0.22398*i
1.7502-0.79880*i	-1.4100+0.22398*i
-1.2288+0.64005*i	-1.2288-0.64005*i
-1.2288-0.64005*i	-1.2288+0.64005*i
0.27267+0.88192e-1*i	-1.1963-0.47577*i
0.27267-0.88192e-1*i	-1.1963+0.47577*i
0.14241	-0.63213
-0.63212	0.14241
-1.1963+0.47577*i	0.27267-0.88192e-1*i
-1.1963-0.47577*i	0.27267+0.88192e-1*i
0.78991	0.32276
1.3738	0.50271
0.32276	0.78991
0.50271	1.3738
-1.4100+0.22398*i	1.7502-0.79880*i
-1.4100-0.22398*i	1.7502+0.79880*i

Table 2.1: Extrema of the chirality measure κ for a specific triangle approximated with Matlab. The solutions for a and b correspond to one another consecutively. For further details see text.

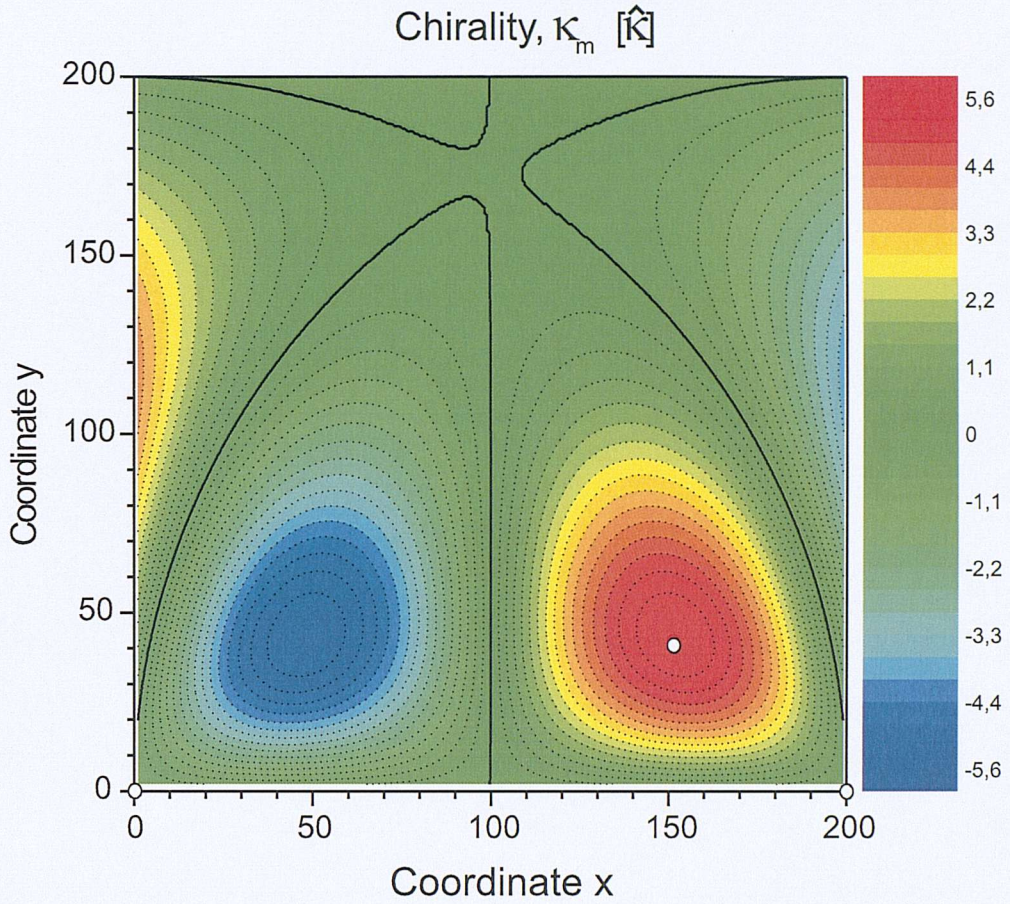

Figure 2.2: The mass-normalised chirality of a triangle with masses 1 in the vertices $(0,0)$, $(200,0)$ and (x,y) shows a maximum for the sketched configuration ($\circ$). Zero chirality is indicated by a thick black line. (Of course these isolines should meet in the top part of the graph which has been crippled by the visualisation software.)

which can be used as a unit of planar chirality for the measure defined by Eq. 2.1. Irrespective of a consideration of κ, κ_a, κ_m or κ_{am} the same fundamental (irrational) number $\hat{\kappa}$ which is dictated by the actual construction of the measure can be used. It will be employed throughout this chapter; additionally, for these abstract considerations, the units of mass and length will be chosen as 1.

In order to communicate the shape of this maximum chiral triangle Fig. 2.2 has been included, where already the Monte Carlo technique to be introduced in the following sections has been used. Of course an equivalent graph could also have been created in a non-iterative process, but it was needed at a different stage for comparison to calculations of more complex structures.

2.1.6 Prospects

The area term of the chirality measure has been introduced because of its crucial influence on the convergence of κ to zero for the limit of a transformation of a scalene triangle into a single point [Potts et al., 2004, lemma 2.4 and postulate 2.5]. This test however would fail if accepting that chirality is independent of the scale of an object. Then convergence of the three points while maintaining their relative positions would simply provide a constant chirality. Latter anyhow is only defined for sets of three points and hence its behaviour for a zero-dimensional object meaningless. Therefore another measure could be created by omitting the area term in Eq. 2.1.

Simulations using the Monte Carlo technique (Sec. 2.2) have shown that this measure shows a very similar behaviour for the examples of Sec. 2.3. It however converges magnitudes faster than the measure discussed here, because it only considers the types of appearing triangles combinations and not their scale. On the other hand it returns non-zero chirality for points on a line. The possible computational gain might outweigh this limitation, particularly for combined physically motivated modifications to the measure. A thorough investigation is pending.

From photonics point of view introduction of an angle dependence to simulate the coupling possibilities for linear or non-circularly polarised light in general and a substitution of the area dependence by a value comparing with the applied wavelength will open new doors. This however would leave the grounds of a purely geometrically motivated and generic chirality measure.

2.2 Measuring chirality using Monte Carlo integration

Research in photonics and particularly the idea of using a measure of planar chirality to categorize surface structures and the related hope to be able to predict their behaviour for light interactions to a certain level stimulated the need for an algorithm and programme being able to calculate the desired values. Not only artificially created templates but also arbitrary images should be valid input to ensure maximum flexibility. When however implementing a direct calculation method for the measure discussed in the previous section along e.g. the lines of Eq. (2.3) its limitations will soon make more dedicated problems unsolvable:

For the case of a 32×32 matrix forming a mesh and containing a mass distribution one would need to consider $(32 \cdot 32)^3 \approx 10^9$ triangle combinations to calculate the chirality measure when applying the original definition, Eq. 2.1. Using modern computers this is a matter of minutes. Yet the requirement for considerably finer meshes for complex objects imposes a limit soon reached, because the number of necessary triangle combinations scales with N^3 for N discrete masses. There are several methods to improve this situation slightly, but only an iterative process can eventually be magnitudes faster in computing a reliable approximation of the overall chirality of a mass distribution.

2.2.1 Monte Carlo method

Many areas of physics use approximation techniques to numerically evaluate integrals which might otherwise not be solvable at all or only after an unacceptable length of time. One of the successful and modern examples is the *Monte Carlo method* [Bartlett, 1964; Jain, 1992; Madras, 2002]. Its main idea in relation to our case is the use of randomly chosen triangle combinations and the probability for a convergence of the calculation far before their number actually reaches the level of all possible triangle combinations within the investigated mass distribution.

2.2.2 Implementation

The construction of a programme complying with the various demands it might face was in itself a task of large scale. It has been realised using an object oriented programming technique for C++ and subdividing the range of problems into classes. A main programme invokes instances of these objects and enhances their communication. This approach allowed a simplified integration of the other ideas like additional parameters and analysis techniques within the now more than a year lasting continuous development process.

It is mainly divided into the areas:

- main programme,
- matrix administration and statistics,
- matrix construction, import and export from and to graphics and ASCII formats,
- generation of random numbers,
- main analytical algorithms,
- generation of standardized templates,
- general I/O (input/output) controls, logging facilities, file access and
- general mathematical operations and constants.

Necessary of course is a thorough optimisation of all involved variables and algorithms to use the least resources possible. Apart from the various small decisions, there have been some major deliberations concerning the randomization process which should be noted in the interest of reproducibility:

The generation of high quality random numbers is crucial for a process depending that much on equidistribution and a long period. The C++-internal clib algorithm is slow in comparison to other modern random number generators. A significant increase in speed has been gained by employing the *Mersenne Twister* developed by Matsumoto and Nishimura [1998].

Furthermore the number of random number generations can be reduced to half than when not choosing each of the six planar coordinates of the three points per combination separately: Instead a list of all nonzero-mass points containing coordinates and masses can be generated so that only one random number is needed to choose the index number of a coordinate. Additionally the chance of involving one or more points with zero mass in a combination is avoided. Latter would automatically lead to zero chirality and is unnecessary surplus.

The programme has two main operational modes which refer to graphics input or artificial matrix creation respectively: Either an image or one of the more than 150 predefined template sets can be chosen. Images are imported using the graphics library ImageMagick[3] enabling the use of all major formats. The matrix is saved using 256 levels which is thereafter exported to a proof file in PNG format. This enables an easily accessible verification of the calculated matrix. Following this step are various statistical measures starting with dimension, area, mass and involving more complex issues like centre of mass and linear regression and correlation.

Afterwards starts the actual approximation process which assumes all values to be unit-less defining the length one by the mesh of the matrix and allowing the mass to vary between 0 and 255. It can be described by[4]:

$$\kappa_n = \frac{1}{12}\frac{N_*^3}{n}\sum_{\lambda\in\Lambda_n} k(\lambda) \quad \text{and} \tag{2.14}$$

$$k(\lambda) = m_i m_j m_k \left(\frac{|\boldsymbol{r}_{ij}|-|\boldsymbol{r}_{ik}|}{|\boldsymbol{r}_{ij}|+|\boldsymbol{r}_{ik}|} + \frac{|\boldsymbol{r}_{jk}|-|\boldsymbol{r}_{ji}|}{|\boldsymbol{r}_{jk}|+|\boldsymbol{r}_{ji}|} + \frac{|\boldsymbol{r}_{ki}|-|\boldsymbol{r}_{kj}|}{|\boldsymbol{r}_{ki}|+|\boldsymbol{r}_{kj}|}\right) \times (\boldsymbol{r}_{ij}\times\boldsymbol{r}_{ik})\cdot\widehat{\boldsymbol{e}}_{\text{obs}}, \tag{2.15}$$

where $\lambda = (i,j,k)$ is chosen from the subset of n triangle combinations Λ_n of all possible triangle combinations Λ possible for the N_* involved nonzero masses within the mass distribution: $\lambda \in \Lambda_n \subseteq \Lambda$ and $|\Lambda| = N_*^3$.

The actual number of triangle combinations n for a real implementation has

[3]For details see: `http://www.imagemagick.org/`

[4]In general of course accidental multiple considerations of a single triangle combination can occur which is not reflected directly by this description.

to be limited by a certain number of maximum calculations $n_{\max}$. Generally it will be unknown how many iterations are necessary to reach a certain accuracy. By not only summing $k(\lambda)$, but also storing the sum of $(k(\lambda))^2$ one can easily use these two values to determine the standard deviation σ of the average κ reached after n steps:

$$\sigma(\kappa_n) = \frac{1}{12}\frac{N_*^3}{n}\sqrt{\frac{1}{n-1}\left(\sum_{\lambda\in\Lambda_n}\left(k(\lambda)\right)^2 - \frac{1}{n}\left(\sum_{\lambda\in\Lambda_n} k(\lambda)\right)^2\right)}. \tag{2.16}$$

Together with an imposed number of maximally to be calculated triangle combinations $n_{\max}$ a set target for the relative standard deviation

$$\sigma_r(\kappa) = \frac{\sigma(\kappa)}{\kappa} \tag{2.17}$$

can form a viable constraint for the duration of the approximation process.

Normalisation techniques

As described in Sec. 2.1.3 and 2.1.4 it is appropriate to additionally deliver normalised values. While mass-normalisation κ_m has been implemented as suggested beforehand, representative areas A are to be determined to allow for κ_a and κ_{am}.

For most cases the area of the smallest rectangle (with horizontal and vertical sides) surrounding all nonzero masses can be considered as a sufficiently accurate approximation, see Fig. 2.3 a. This approach has been used throughout this chapter and is denoted with the earlier introduced index a: κ_a and κ_{am}.

There are however cases where e.g. background noise within a picture introduces a much larger than necessary area. The investigation of galaxies in Sec. 3.3 particularly suffered from this approach. As galaxies mostly have elliptical shape or at least an elliptical area defining the space it occupies, an according algorithm has been developed, see Fig. 2.3 b:

In order to determine the elliptic area as the product of π and the two

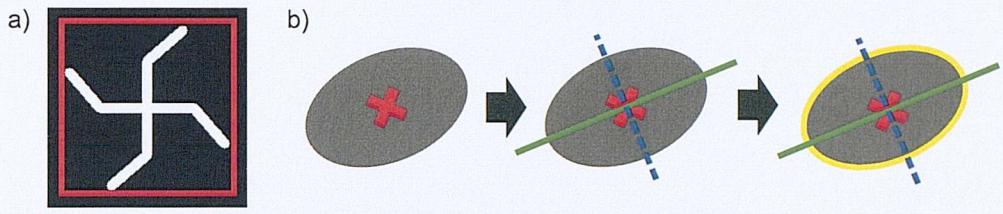

Figure 2.3: (a) Area normalisation uses the the area of the smallest rectangle fitting around a PCS. (b) Elliptical objects like e.g. many galaxies can be normalised using an elliptic area: First the (mass-) centre is calculated. In a second step linear regression delivers the axes of the ellipse. Finally the standard deviations relative to these axes provide the lengths of the elliptic half axes and define the last missing parameters of the ellipse.

half-axes of the ellipse several steps have to performed. Initially the centre of mass is determined to find a rough approximation of the centre of the galaxy. Afterwards linear regression with the origin of its coordinate system within the centre of the galaxy and assuming the fitted straight to pass through the same is performed to determine the direction of the larger axis. Integration over all masses to determine the standard deviation of the weighted distance of the masses in respect to both axes follows. These standard deviations proved to be a suitable representation of the areas occupied by the galaxies in comparison to what an intuitively chosen ellipses would cover. This allows a differently area-normalised chirality denoted with an index e: κ_e and κ_{em}.

2.2.3 Discussion

Two main issues govern the precision of measurements obtained with this method: Convergence and discretisation. Latter imposes limits of feasibility, because a finer mesh automatically results into a considerable increase of the maximum number of triangle combinations: The more complex objects are, the greater the subset will have to be to sufficiently approximate the overall chirality measure.

The convergence criterion $\sigma_r(\kappa)$ appears to suggest an accuracy which is about 4 magnitudes higher than actually reproducible when comparing inde-

pendent approximations. Experience has shown that to reach an accuracy of about a percent the target for the relative standard deviation has to be set in the region of 10^{-6} to 10^{-7}. Another notable general observation is the fact that objects of less chirality than others in most cases converge slower in terms of $\sigma_r(\kappa)$. Hence a large $\sigma_r(\kappa)$ when reaching the maximum amount of iterations can implicate a near zero chirality.

2.2.4 Summary

An optimised algorithm using the Monte Carlo technique to calculate the chirality measure has been developed. It enables the accurate planning of future productions of planar chiral nanostructures within the author's group. Moreover a general tool being able to process many kinds of input is available for other and general investigations of planar chirality. It has been created in a modular way to allow future extensions which could target the area of physically motivated values, introducing e.g. wavelength dependence to weigh chirality.

2.3 Forms of chirality

The application of the algorithm and computer programme developed in the previous section allows to consider various complex planar chiral structures in discretisations levels far exceeding those possible with direct calculation methods. There are several interesting observations to be made:

- When choosing a certain way of describing an object (vertices, lines or solid body) the chirality measure results into considerably different magnitudes and shows largely differing convergence behaviour.
- It is possible to distinguish two kinds of chirality and furthermore possible to describe the chirality displayed by regular grids in terms of *nearest-neighbour* relations, a concept which is applied in many areas of physics.

This section is dedicated to explore these issues and to follow the development of chirality for increasing complexity of the structures. The example structures are motivated by the nanostructured samples that have been created for photonics

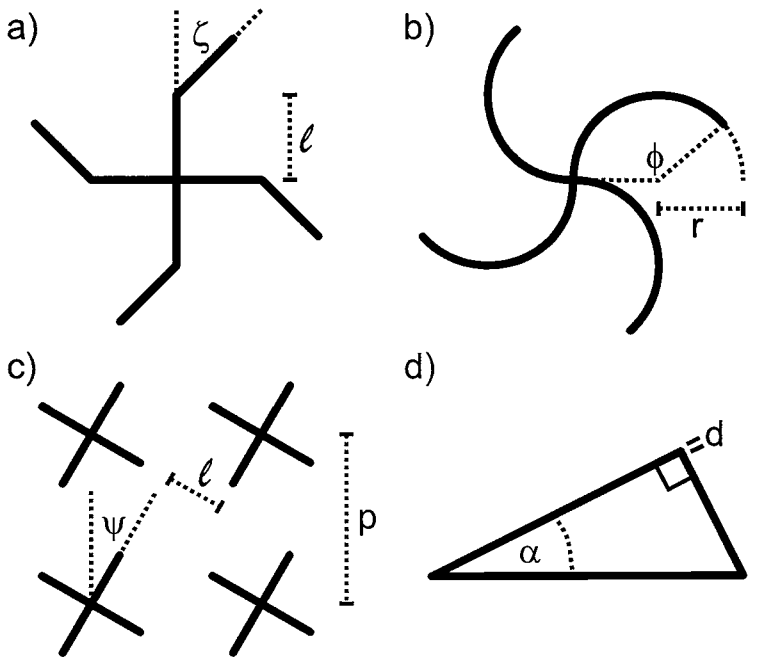

Figure 2.4: The main structures referred to are defined by various parameters: All have the thickness d of the lines defining the structure in common. (a) A bar-gammadion or short gammadion is defined by its eight equal arm lengths l and four bending angles ζ. (b) A round gammadion is defined by the radius r of the involved circles and the angle ϕ to which they are drawn. (c) Tilted crosses are defined by the lengths of the four involved sides l and their tilt angle ψ. All structures arranged in a regular square grid have a well defined pitch p. (d) Perpendicular triangles will be described by a variation of one of their angles α.

research within the author's group. The structural definitions are depicted in Fig. 2.4. For all shown calculations the mass of a matrix entry / intensity of a pixel is either one or zero: The possibility of further levels will not be used in this section.

2.3.1 Structure representations

The choice of representing an object either by points in its corners, lines defining its borders or a solid body has various implications on the chirality measure and

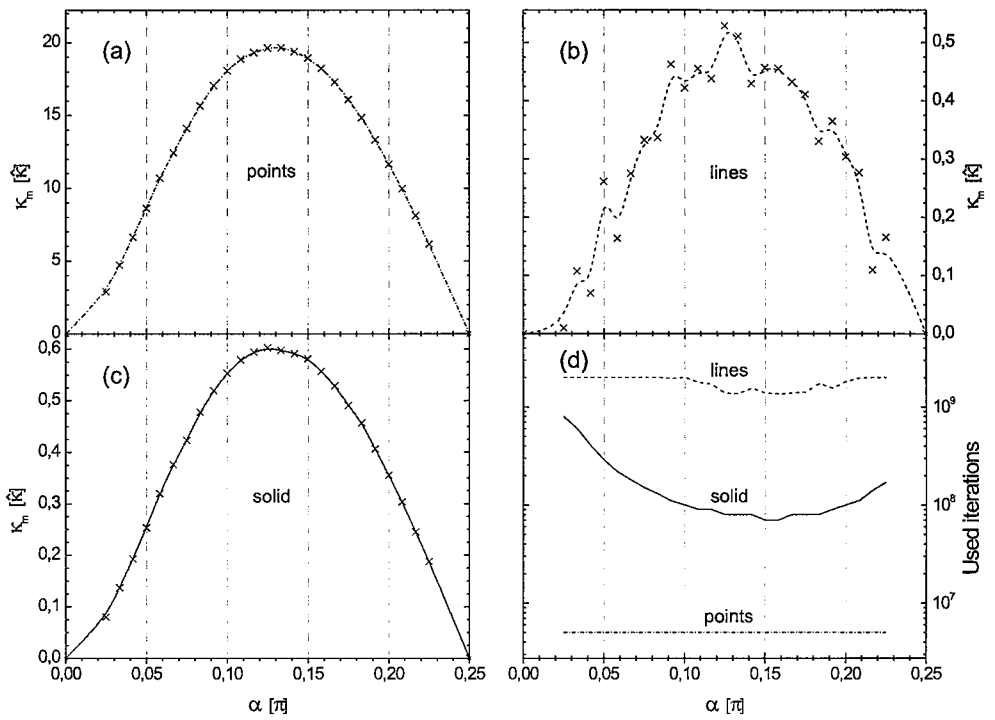

Figure 2.5: The different geometrical representations of a perpendicular triangle display differing chiralities κ_m and convergence behaviour for a variation of one of its angles α while keeping its area constant at $A = 50000$ units (pixels / mesh points).

its approximation. The basic concept can easily be understood at the example of a perpendicular triangle in which one angle is changed while the overall area is kept constant, see Fig. 2.4 d.

The results according to the three approaches are depicted in Fig. 2.5: While the triangles made of three points naturally converge within a minimum amount of calculations (until convergence is tested for the first time), a representation by lines has the poorest convergence behaviour. Yet it has to noted that the relative maximum and development of chirality is equal in all cases. Most notably is the nearly equivalent amplitude for the 'lines' and 'solid' cases after mass-normalisation. Another result of more general importance is the derivation of the maximum chiral perpendicular triangle being found for a triangle

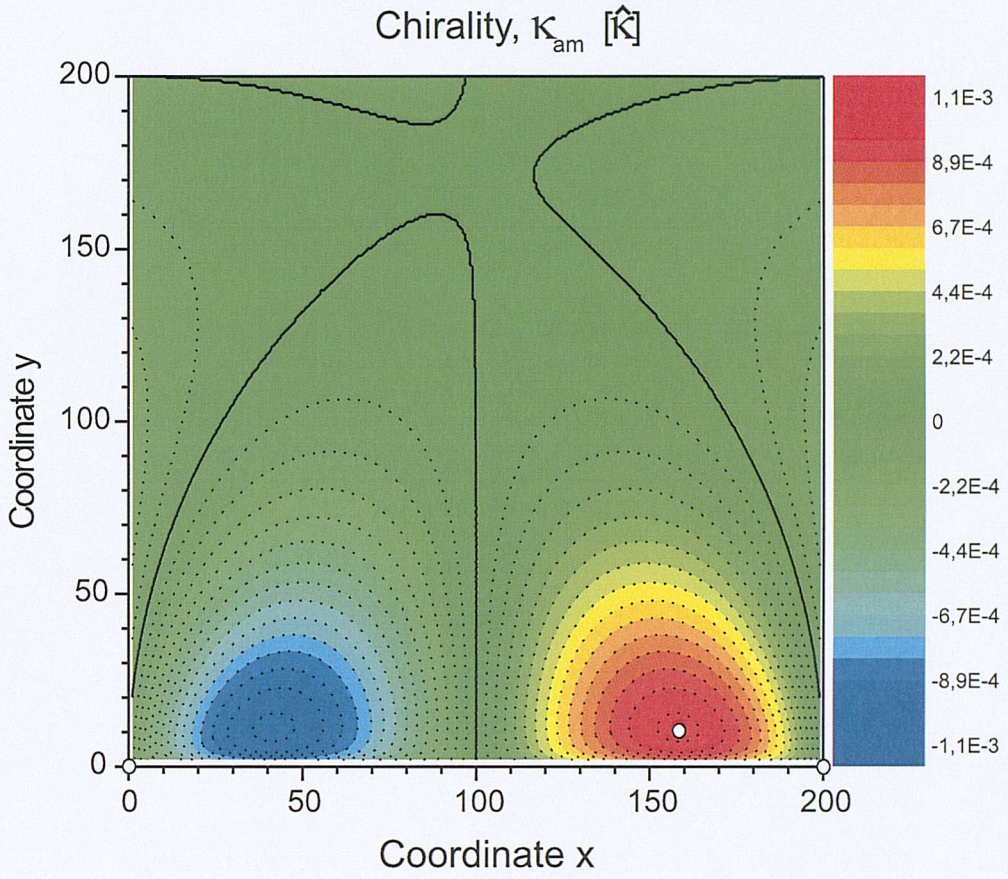

Figure 2.6: Mass and area normalised chirality κ_{am} in units of $\hat{\kappa}$ of an arbitrary shaped triangle defined by points in its corners (○): Coordinates $(0, 0)$ and $(200, 0)$ are fixed while the position of the third one (x, y) is changed. The shape of a triangle displaying maximal chirality is shown. Zero chirality is indicated by a thick black line. (The visulisation software introduced an error on top: The zero isolines should meet and not avoid one another.) See also Fig. 2.2.

with an angle α of around 22.5°.

For arbitrarily shaped triangles one needs to approximate the chirality of a huge number of triangles to resolve the general behaviour, see Fig. 2.2. A comparison with the area- and mass-normalised chirality κ_{am} shows a much smaller and differently shaped triangle for the maximum and minimum configurations, see Fig. 2.6. Solid triangles have been investigated along exactly the same lines

and intriguingly an equivalent behaviour with extremal values for equal shapes has been found.

2.3.2 Primary (molecular) chirality

Chirality is often sub-categorised into a part which stems directly from an individual object and another one resulting from the structural arrangement of objects in relation to one another. Latter is introduced as structural chirality and could also be called *secondary*. This distinguishes from the molecular chirality of a single object which must be the starting point of any investigation, hence denoted here as *primary*. This section develops the main concepts necessary to correctly interpret chirality approximations and discusses various objects of interest when considered alone.

Triangles

... have already been introduced and discussed in the previous section and their main properties can be found in Fig. 2.2 and 2.6.

Γ–type and (bar-) gammadion structures

The (bar-) gammadions which have been the driving force of the recent advances on light matter interactions of planar chiral nanostructures [Papakostas et al., 2003; Schwanecke et al., 2003] can be broken down into four equal structures formed by two lines of (generally) unequal length which are connected in one of their ends.

These Γ-*type* structures display three configurations with maximum or minimum chirality for line lengths which are roughly of the same magnitude, see Fig. 2.7. Intriguingly the arrangement in a fourfold rotational structure to form a *bar-gammadion* or *gammadion*[5] results into a different dependency on the relative variation of length and mutual orientation of the composing lines, see Fig. 2.8. The sign change of chirality for large (x, y) in comparison to Fig. 2.7

[5]The lone word *gammadion* will in due course only be used to refer to *bar-gammadions*.

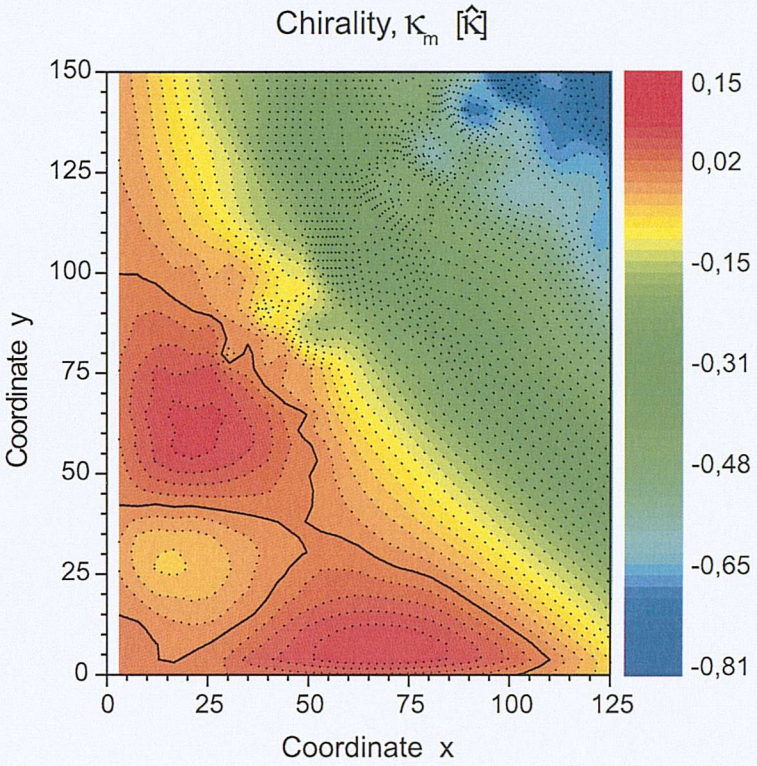

Figure 2.7: The chirality κ_m of a Γ–type structures consisting of two lines connecting each of the coordinates $(0,0)$ and (x,y) with $(0,50)$ shows considerable substructure: Three extrema can be found apart from the general decrease (but absolute increase) in chirality for large x and y. Zero chirality is indicated by a thick black line.

should also be noted. This serves as a general example of how distinct the behaviour of the chirality measure alters as soon as new objects are introduced, even when they equal one another and are arranged symmetrically.

For the mentioned research of greater importance is the analysis of bargammadions where all branches are of equal length and a variation solely of the bending angle is considered. This is the way most of the available samples have been constructed. Figure 2.9 displays the results of approximations which used a design roughly resembling the samples described in Papakostas et al. [2003]; Schwanecke et al. [2003] with a ratio of $l : d = 5 : 1$, for the definition see Fig. 2.4.

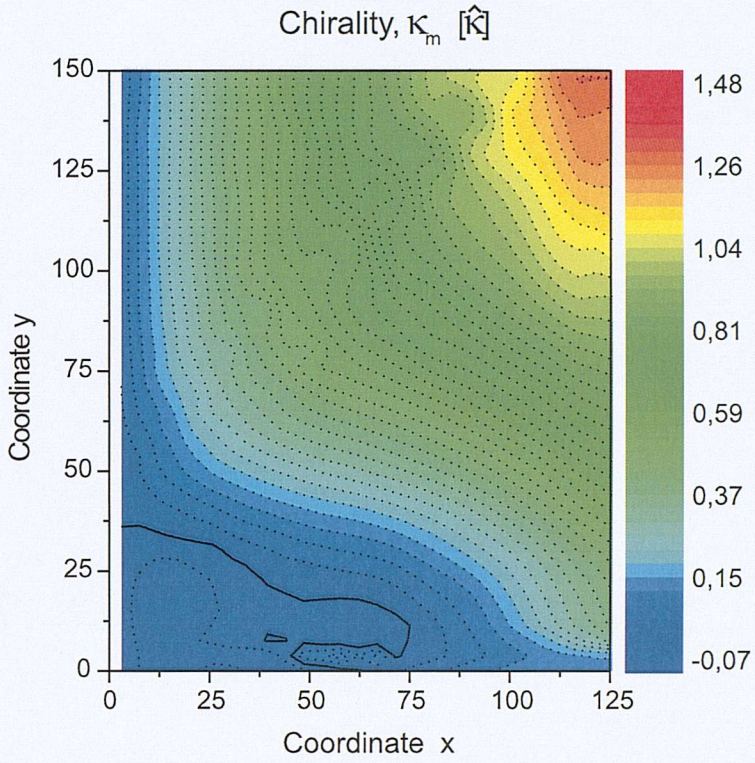

Figure 2.8: The chirality κ_m of an unequal sided 4-fold gammadion, extending the form of the structures measured for Fig. 2.7 contains considerably less structure: Only two areas with chirality of different sign can be seen. Zero chirality is indicated by a thick black line. This plot also contains a good example of possible discretisation artifacts: The wave-like disturbances between the coordinates $(0, 50)$ and $(100, 150)$ stem from fewer points and lower mass respectively that lines occupy when discretised at an angle of 45°.

Using this graph a basic concept for the interpretation of the measurements can be derived: The unnormalised chirality κ does not show show a completely smooth behaviour. This stems from the varying masses m involved in the discretisation of the various configurations. The mass-normalised chirality κ_m can eradicate this cubic effect to a large extent and should be considered the main result of any approximation. The area-normalised chirality κ_a requires the same treatment resulting into the fully normalised chirality κ_{am} which

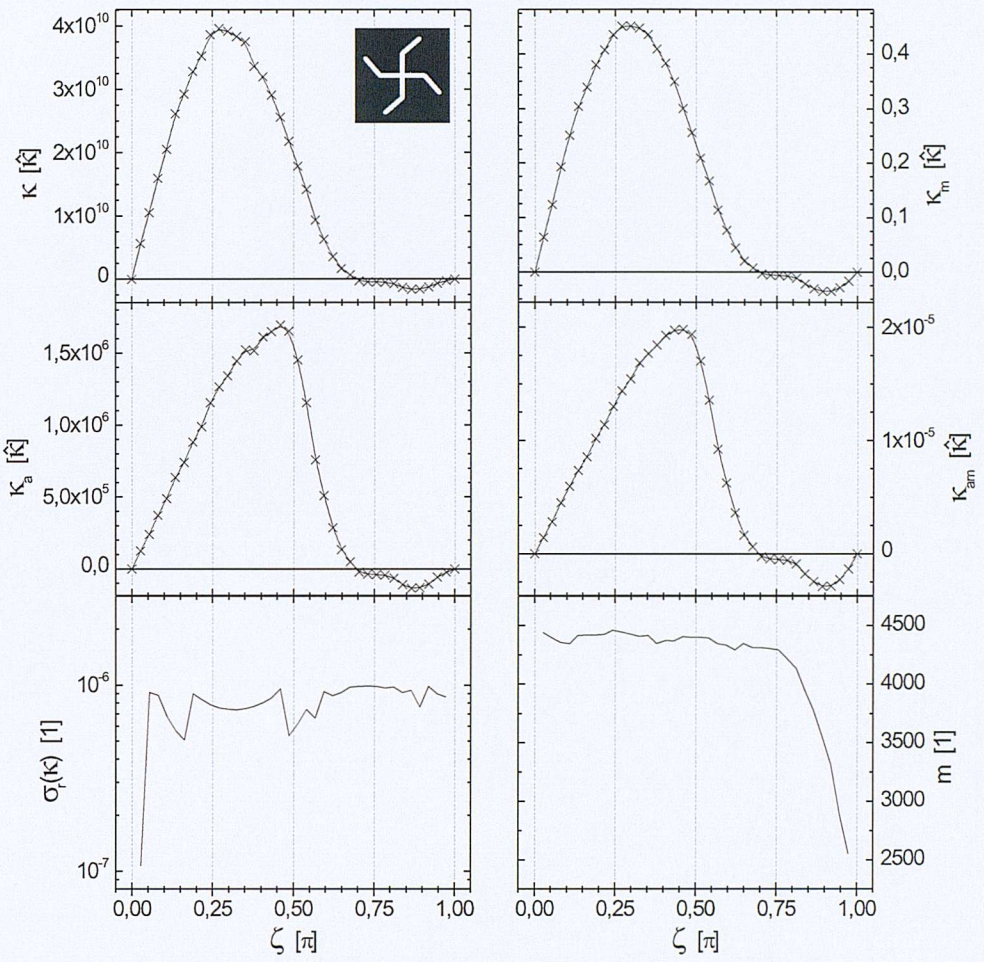

Figure 2.9: A sensible discussion of the chirality κ of a *gammadion* and a variation of its bending angle ζ requires the consideration of various parameters: *i*) the influences of applied normalisations κ_m, κ_a and κ_{am}; *ii*) the acquired level of accuracy represented by $\sigma_r(\kappa)$; *iii*) and the discretisation process which is represented by the sum of the masses (or pixels) describing a certain design. The design parameters are $l = 50$ and $d = 10$, see Fig. 2.4. The main features to note are the defined maximum of κ_m around $\zeta = 0.3\,\pi = 54°$ and the inversion of the sign for large bending angles.

furthermore can be used to discuss the matter of close packing while κ_a can be ignored. Additionally the reached accuracy has to be checked: Here a target of $\sigma_r(\kappa) \leq 10^{-6}$ was set which has been reached for all approximations within the set amount of maximum triangle combinations $n_{\max}$.

The characteristic features are the near quadratic evolution for small and medium sized bending angles with a well defined maximum for κ_m around $\zeta = 0.3\,\pi = 54°$ and its sign change around $\zeta = 0.68\,\pi \approx 122°$ with a relatively small minimum around $\zeta = 0.9\,\pi = 162°$. This intuitively unexpected inversion of the sign of chirality can actually be perceived subjectively for drawings of gammadions with different bending angles: The twist one would associate with these structures changes direction. An illustration of this situation can be found in Fig. 5 b/c of the article by Potts et al. [2004]. Similar results have previously been gained by Papakostas et al. [2003]; Potts et al. [2004] employing direct calculation of the chirality measure.

Round gammadions

Stimulated by calculations made by Professor Prosvirnin describing light matter interactions of small metallic wires of circular shape to represent the gammadions and the work on non-reciprocity [Prosvirnin and Zheludev, 2003] a round gammadion type has been investigated, see Fig. 2.10. The comparison of its properties with the bar-gammadions will show similarities as well as distinct differences:

Here the object increases its mass m roughly linearly with increasing defining angle ϕ. This affects the chirality strongly which can be seen by a comparison of κ and κ_m. The furthermore increasing occupied rectangular area for $0 \leq \phi \leq \pi$ gains significant influence on the behaviour of κ_{am}. These distinct differences make a physical similarity to bar-gammadions unlikely or are at least not easily motivated.

However the characteristics of a bell shape and an inversion for high angles resemble a bar gammadion vaguely. Please also note that $0 \leq \zeta \leq \pi$ for a gammadion while $0 \leq \phi \leq 2\,\pi$ for a round gammadion which results in differently scaled x-axes for the figures.

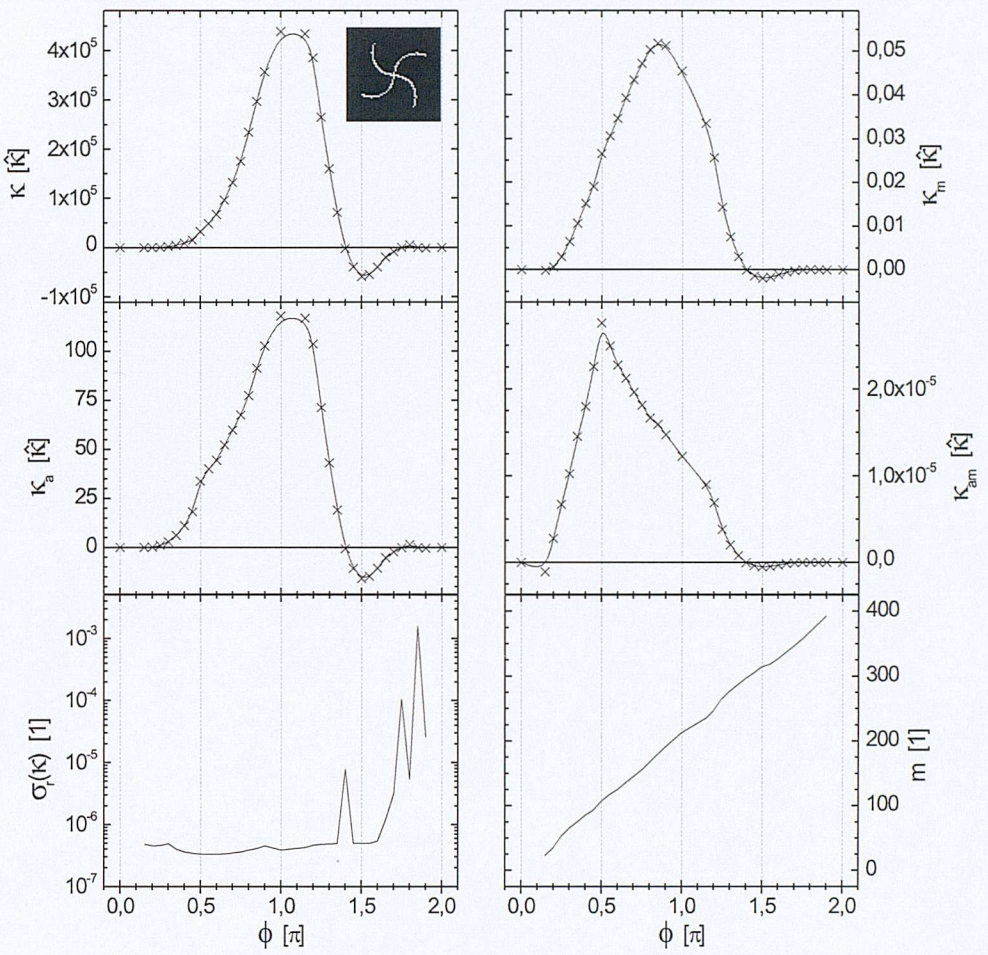

Figure 2.10: The chirality of a *round gammadion* in relation to its defining angle ϕ is alongside the involved masses m and plotted for the design parameters $r = 15$ and $d = 1$, see Fig. 2.4.

2.3.3 Secondary (structural) chirality

The second kind of chirality stemming from the relative arrangement of individual objects has important implications for light matter interactions where the distance of the individual objects is considerably smaller than the wavelength of the light. On the other side diffraction experiments on planar chiral structures have first been predicted and finally been shown to result into much

larger optical activity than for sub-wavelength structures [Papakostas et al., 2003; Vallius et al., 2003] and their interpretation might also benefit from these results.

Naturally a desire for measurements of the chirality of arrays arises which can finally be satisfied by use of the Monte Carlo method allowing appropriately dense discretisation meshes. Once again the main structures of interest, namely gammadions and round gammadions, will be discussed.

Countless areas of physics use the approach of discussing nearest-neighbour configurations which will in due course be found as essential for the description of the chirality of complex arrangements. It will be of particular interest for the estimation of the relative behaviour of arrays containing infinite or large numbers of equal objects. Latter of course is the case for the structures investigated in Sec. 3.1 and 3.2 where 1mm^2 is covered with tiny gammadion structures of few micrometers size.

Yet beforehand, in order to consistently follow the trail of complexity for chirality, it will be shown how an achiral object can exhibit chirality when arranged in a grid.

Crosses

While an individual cross does not exhibit any chirality as it is its own mirror image, its arrangement in a regular square grid creates not only a subjective perception of twist, but also a chiral structure for most configurations, see Fig. 2.11 a. Naturally tilt angles ψ with $\psi_n = n \cdot \pi/4$, $n \in \mathbb{Z}$ result into self-enantiomeric structures with zero chirality. So a disussion of the range $0 \leq \psi \leq \pi/4$ will already be comprehensive.

Irrespective of the size of the array (having considered arrays of up to 5×5 crosses; not shown) the shape and sign of the dependence stay the same as in Fig. 2.11 a. Please note the fact that less complex structures display higher chirality κ_m (Fig. 2.11 b) which has been found for all arrangements of objects that have been investigated.

For the first time the discussion of nearest neighbours will be applied: It suggests that the lone arrangement of two next neighbours results into a higher

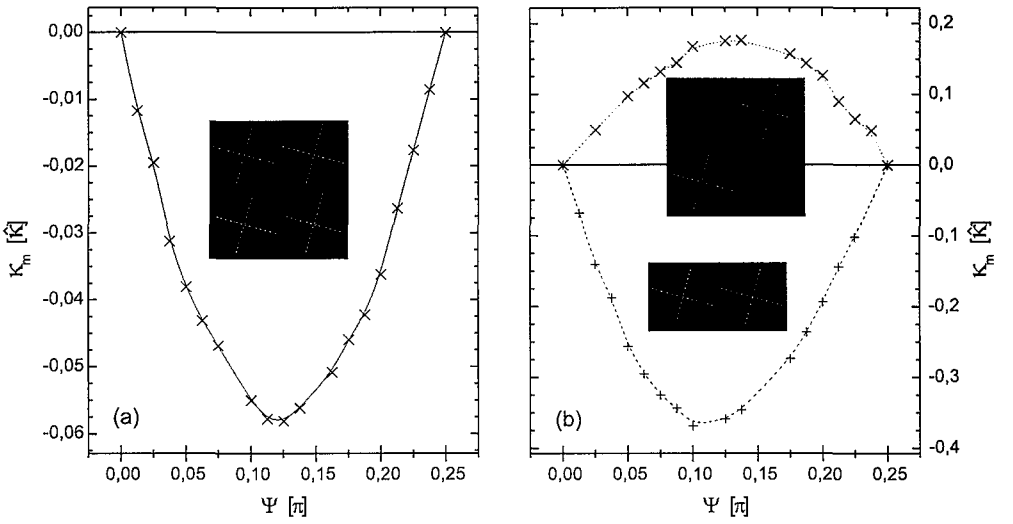

Figure 2.11: The chirality for arrays of tilted crosses and the first two nearest neighbour configurations with tilt angles ψ is plotted for the design paramaters $l = 80$, $d = 1$ and $p = 165$, see Fig. 2.4.

absolute chirality (Fig. 2.11 b, bottom graph) than the consecutive diagonal placement involving a larger distance (top graph). However the relative shape of the graphs in both plots stays the same and it appears that the mutual influence of crosses positioned along the axes of the grid is higher than of those positioned diagonally. Particular indication is the equal sign of the graph in plot (a) and bottom graph of plot (b). Of course this discussion is far from general, but the consideration of further structures will back up this approach.

Bar gammadions

Figure 2.12 depicts the chirality variation for the first three nearest-neighbour configurations of gammadions in a regular square grid. Once again it can be observed how more complex structures arrive at lower mass-normalised chiralities κ_m, see particularly Fig. 2.12 a.

Experiments have shown that the rotation of the polarisation azimuth of light for large bending angles does not change sign while the chirality of a single gammadion does [Papakostas et al., 2003, Fig. 2 d]. The configuration

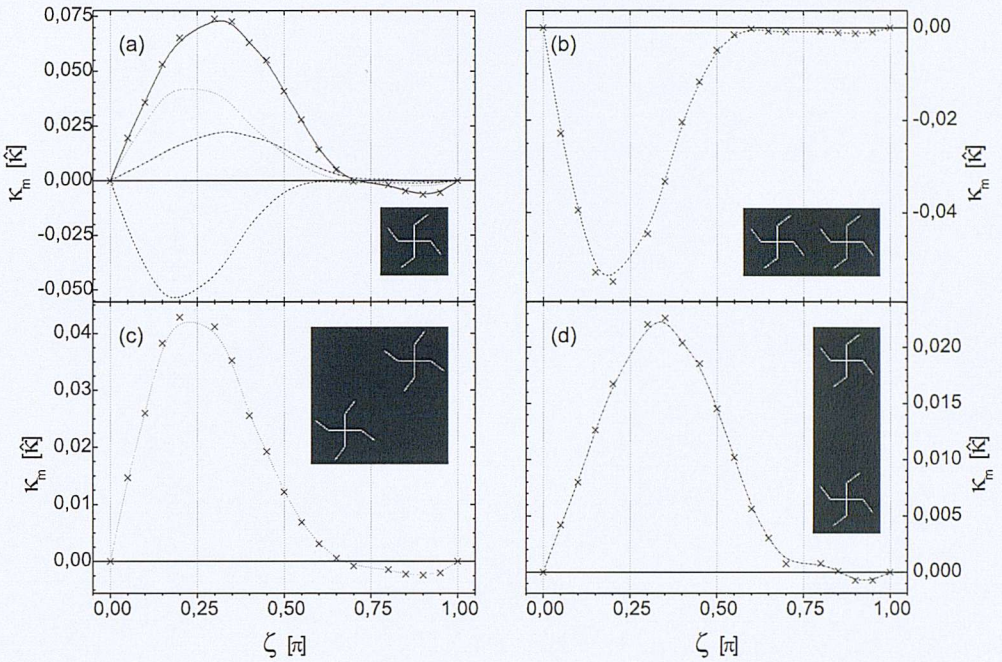

Figure 2.12: The chirality of *gammadions* and its relation to the bending angle ζ are plotted in various nearest neighbour configurations (b-d) for the design parameters $l = 20$, $p = 45$ and $d = 1$, see Fig. 2.4. Plot (a) serves the comparison of these graphs to the single gammadion chirality (solid line).

in Fig. 2.12 b however might be a description of the main influence leading to these results for the first order diffraction experiments and might stimulate further experimental investigation.

The nearest-neighbour combinations are finally put into the context of large arrays by Fig. 2.13. When comparing Fig. 2.12 b with Fig. 2.13 d and Fig. 2.12 c with Fig. 2.13 f one is instantly forced to note their intriguing similarities. Apart from tiny discrepancies (which can approximatively be described by influences of the further neighbours shown e.g. in Fig. 2.12 d) they are just scaled versions of one another. Plots (d) and (f) have been artificially created to each emphasize one of the first nearest-neighbour 'interactions'[6].

[6]While this physical term might be out of place, it is helpful to communicates the idea of the concept.

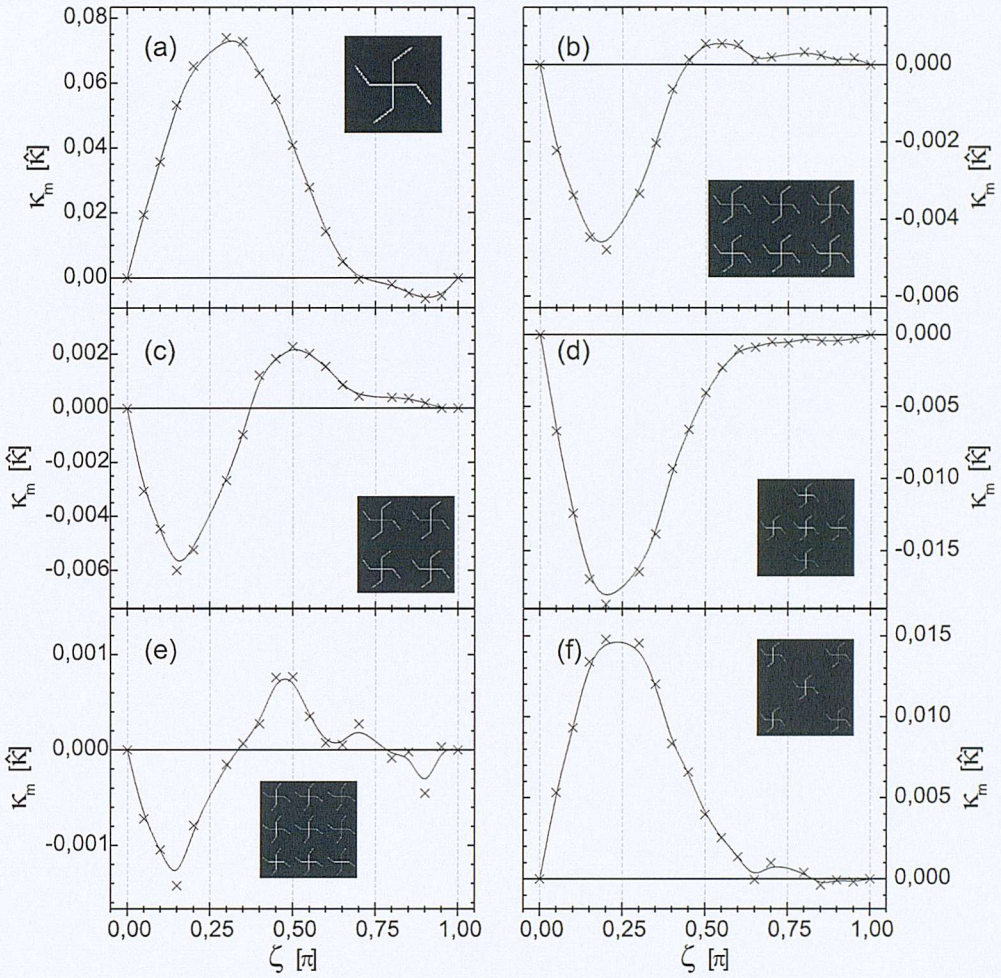

Figure 2.13: A number of further *gammadion* configurations add to the chirality approximations of Fig. 2.12.

To summarise, despite larger and more complex configuration one can find the influence of the dominant nearest-neighbour configurations. In a next step complete arrays, like 2×2 and 3×3 arrangements have to be put into the picture. In order to simplify the terminology the configurations depicted in Fig. 2.12 will be named *straight* for part (b), *diagonal* for part (c) and *far* for part (d). The 2×2 array of Fig. 2.13 c contains 4 straight, 2 diagonal and no far combinations while the 3×3 array of Fig. 2.13 e features 12 straight,

8 diagonal and 6 far combinations[7] of the individual gammadions. The same dominance of the straight combination of course continues for larger arrays.

This allows to discuss several bending angle regions of Fig. 2.13 c (and e). While initially the straight combination dominates, its relatively quick decline to zero in comparison to the diagonal and far combinations allow the sign change around $\zeta = 0.35\,\pi = 63°$ and the maximum shortly afterwards. All combinations decline to zero for large bending angles which resembles the behaviour of both arrays.

The noise appearing for the 3×3 array serves as a good example of how the limitation to a maximum number of random triangles $n_{\max}$ can limit the acquired accuracy, here reaching $\sigma_r(\kappa) \approx 10^{-5}$ for $n_{\max} = 3 \cdot 10^9$. This limit is not far away from the presently justifiable limit to be drawn somewhere between 10^{10} and 10^{11} random triangles per approximated example considering actual execution times.

Additionally the sensitivity of the combined chirality of two gammadions to their distance should be noted: It even leads to a chirality sign change for their doubled distance depicted in Fig. 2.12 b and d. The possibility of specific distances which lead to near zero chirality over large ranges of the bending angle variations which is suggested by the continuity of the chirality measure will have to be investigated.

Round gammadions

The chirality approximations of arrays of round gammadions were stimulated by a search for near zero chirality and a possible sign swap around $\phi = \pi/2$ as for the nonreciprocal difference [Prosvirnin and Zheludev, 2003, Fig. 3, bottom part, inset]. While Fig. 2.14 c and d suggest a developing minimum in that region allowing zero chirality, an overall sign swap of the chirality appears to be unlikely for large or infinite arrays.

Here again nearest-neighbour considerations can be applied using Fig. 2.14 a and b as a basis for the *straight* and the *diagonal* combination. However their actual combination, shown in Fig. 2.14 d, appears to be more significant in this

[7] The two 'far diagonal' combinations will be ignored at this point.

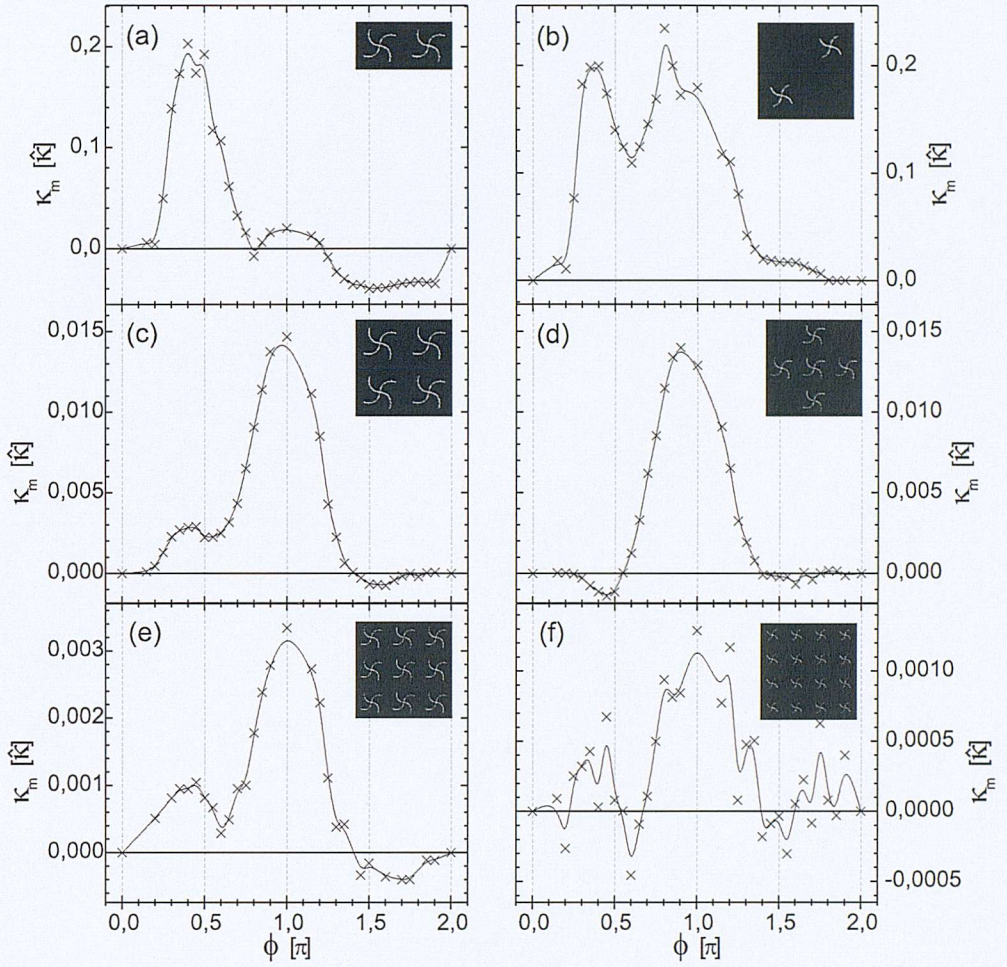

Figure 2.14: Complementing the two previous graphs, here the chirality of various configurations of *round gammadions* with the design parameters $r = 15$, $d = 1$ and $p = 65$. Additionally compare to Fig. 2.10 containing results on a single round gammadion.

case, see parts (c) and (e). A large maximum around $\phi = \pi$ manifests itself while the growing influence of the straight combination enlarges the first local maximum around $\phi = 0.4\,\pi = 72°$. At the same time a local minimum between these maxima becomes more distinct. In any case the sign reversal for large ϕ already seen for the lone round gammadion remains, compare Fig. 2.10.

Here as well another example for the convergence of the approximations in relation to the array size and number of maximum allowed random triangles $n_{\max}$ can be seen: For a 3×3 array and $n_{\max} = 10^9$ the accuracy is quite high, while the approximations of 4×4 arrays with $n_{\max} = 3 \cdot 10^9$ contain considerable noise, see Fig. 2.14 e and f. For latter particularly the low chirality of large defining angles ϕ is resolved badly, which again reminds of the coincidence of low chirality and high relative standard deviation after the same number of calculations.

2.3.4 Conclusions

For various examples, which have been particularly motivated by current research, the trail of chirality and its development for increasing complexity has been followed. A significant amount of data which can be compared to experimental and numerical data of existing and future material configurations has been provided, where the results shown here only provide a snapshot summarising the evolved ideas and most important results. At the same time concepts have been introduced which allow to understand the chirality of composite PCS: The initial approach dividing into primary and secondary chirality is followed by the discovery of the applicability of nearest-neighbour consideration for chiral arrays.

3 Application of the Chirality Measure to Photonics and Image Analysis

The past chapter was dedicated to a general and theoretical discussion of planar chirality and set its measure apart from its actual appearance and implications in non-abstract contexts. The main driving spirit for this investigation in the first place was to establish a measure which thereafter could be used to help predict the level to which nanostructured surfaces could interact with light, particularly in the visible and near infrared region of the spectrum. On the other hand the general influence chirality might have on the symmetries governing light-matter interactions are largely unexplored. This chapter tackles these issues and reports initial but striking findings. Matters like the inheritance of substrate chirality to its diffraction pattern and time non-reversal will be discussed.

Furthermore the viability of the planar chirality measure, as well as its combination with the Monte Carlo method, as an image analysis method will be tested. The example of spirality exhibited by galaxies will be used as a testing ground. In combination with dedicated normalisation techniques it will be shown that it constitutes an applicable tool with a straightforward algorithmic definition and might improve parts of the morphological classification schemes used by astronomers.

3.1 Diffraction pattern

Last year two independent publications showed how planar chiral structures can affect the polarisation state of light. Both used arrays of the four-fold gammadion type structures which have been introduced in Fig. 2.4 (p. 24):

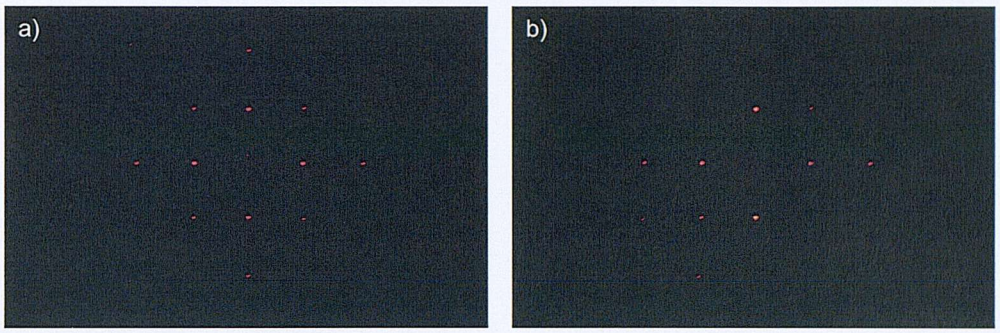

Figure 3.1: Observed diffraction patterns. display rotational symmetries (a) and exhibit a sense of twist or chirality for certain experimental configurations (b). (The diffraction pattern may not be seen well for some printers, refer to Fig. 3.8 instead.

Using sub-wavelength sized elements Vallius et al. [2003] were able to detect azimuthal polarisation rotation of linear polarised light of up to 2.2° for zero-order transmission. Theoretical considerations allowed them to predict up to 4° of rotation near resonances within the visible spectrum. The seen effect is even more pronounced for preceding diffraction experiments on structures larger than the probing wavelength [Papakostas et al., 2003]. They found the absolute rotation exceeding 30° for certain experimental configurations. Latter experiment was able to establish a first link to the proposed chirality measure which was later published in a more comprehensive discussion by Potts et al. [2004], focus also of the previous chapter. It has to be noted that not only the polarisation azimuth was rotated, but ellipticity was created as well.

As Papakostas et al. [2003] only considered first order diffracted beams the natural next step was to include further ones. This opened up several new possibilities. Diffraction patterns of PCS show a complex structure which in itself leads an observer to perceive a sense of twist, see Fig. 3.1. In other words it exhibits inherent chirality. Relating the chirality of a diffraction pattern to that of the underlying structure will be one of the central topics of the upcoming analysis. However, the DPs display rotational symmetries as well. Therefore a more general availability of quantitative symmetry parameters, alongside with possibilities to compare them to one another, is desirable. Particularly a

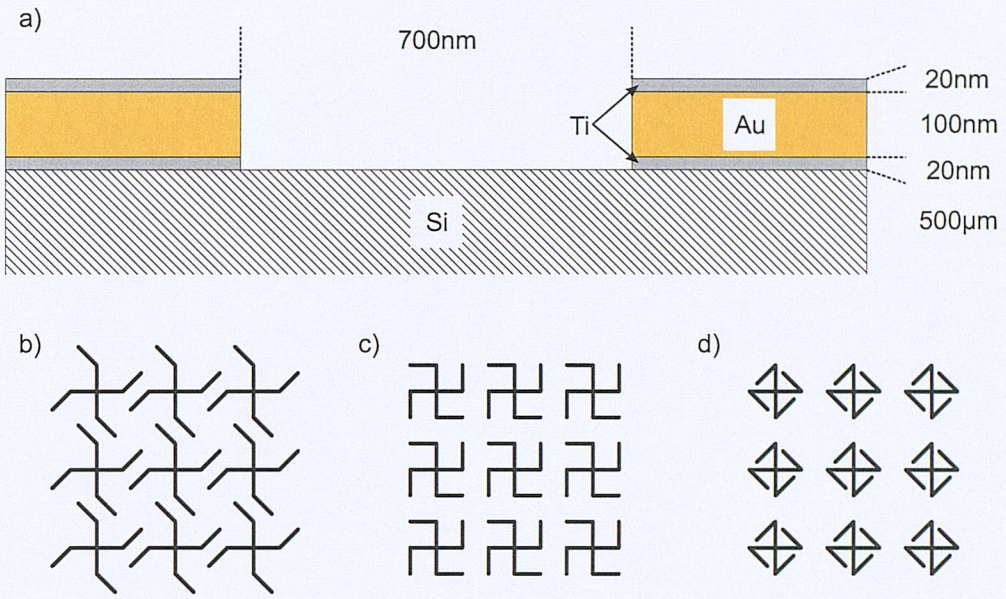

Figure 3.2: (a) Investigated samples consist of metallic layers deposited on Si wafers where grooves in the metal form the structures. (b-d) Three main types of gammadion arrays (and their enantiomers) have been investigated: The sketches depict a variation of the bending angle maintaining constant pitch and arm length.

discussion of the plane-enantiomeric symmetry is imperative for PCSs.

In order to achieve these goals, several analytical techniques had to be developed and combined. After an introductory description of the used experimental setup, their construction will be discussed in detail followed by an analysis of the results.

3.1.1 Experimental setup

The investigated planar chiral structures are arrays of gammadion type structures with bending angles of $\zeta = \pm 45°$, $\pm 90°$ and $\pm 135°$, see Fig. 3.2 b-d. They have been manufactured using a combination of direct-write electron beam lithography and ion beam milling. The actual gammadion structure is formed by grooves in a metallic layer which is situated on a crystalline double-polished silicon wafer. The metallic layer consists of 100 nm of gold surrounded by 20 nm

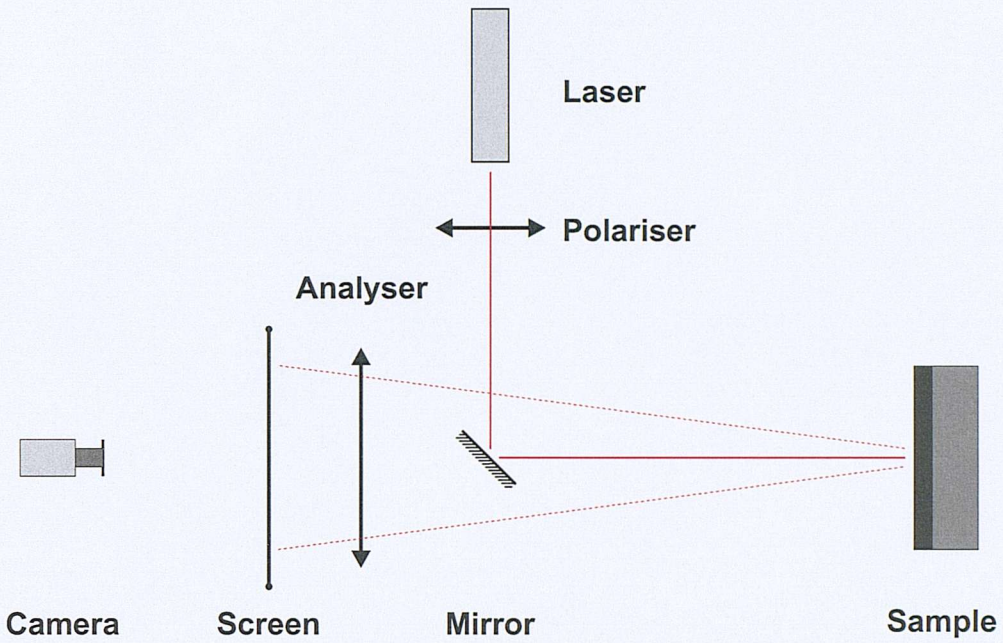

Figure 3.3: Light of a 633 nm He-Ne laser passes a variable linear polariser and is reflected on a sample containing planar chiral structures. Diffracted light is analysed by a second linear polariser before hitting a $10 \times 10\,\mathrm{cm}^2$ ground glass. Image capturing is performed by a CMOS camera.

of titanium on each side, see Fig. 3.2 a. This type of so called 'negative' design is repeated in a regular square array of pitch $p = 4\,\mu\mathrm{m}$. Using the terms introduced for gammadions in the previous chapter, they have an arm length l of $1.4\,\mu\mathrm{m}$ and a thickness d of about 700 nm, analogous to those used by Papakostas et al. [2003].

Visible light at wavelength $\lambda = 633\,\mathrm{nm}$ emitted by a He-Ne laser is selectively transmitted by an initial linear polariser and directed at normal incidence upon the planar chiral surface, see Fig. 3.3. The diffracted beams are analysed using a second rotating polarisation filter situated in front of a $10 \times 10\,\mathrm{cm}^2$ ground glass. A Canon EOS D60 low-noise CMOS camera captures the formed image within controlled exposure times. In substitution of the camera and ground glass either an intensity detector or a polarisation state sensitive detector have been deployed for comparison. It has to be noted that the zero-order beam

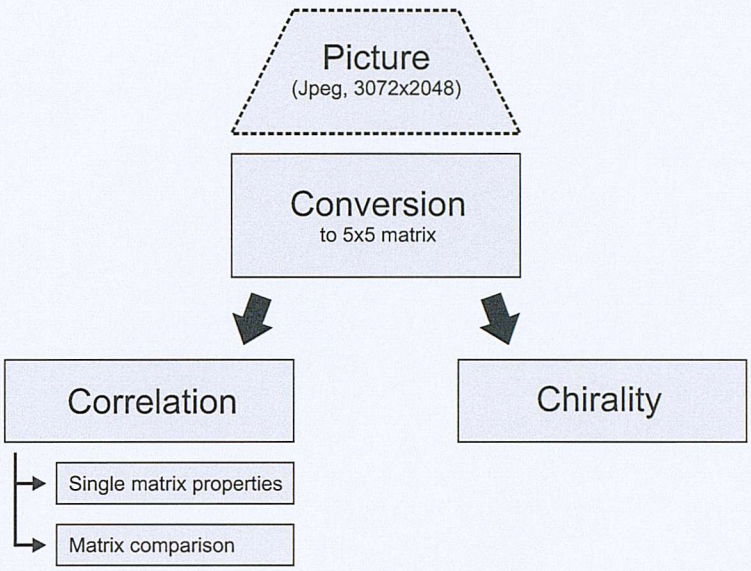

Figure 3.4: The data processing involves several steps and analytical methods: After the initial conversion individual symmetry parameters and comparisons to corresponding configurations are obtained.

is blocked by the central mirror. Therefore its intensity cannot be detected and is arbitrarily assumed to be zero within all upcoming considerations and calculations.

3.1.2 Analytical methods

Using intensity or polarisation state detectors to measure individual diffraction orders requires a considerable amount of time and elaboration of the employed positioning system. Several parameters, non the least precise angular alignment are crucial to ensure reliable measurements. In order to measure chirality within the diffraction pattern one has to include a sufficient amount of diffraction orders. This is not only necessary in order to get a representative set of data, but also to enable point combinations forming scalene triangles, hence allowing nonzero chirality, which only few combinations of first order beams comply with, cp. Sec. 2.1.4.

These considerations stimulate the desire for a method which can easily be

applied to a large number of configurations. Furthermore, the perspective of future intensified production of chiral arrays with shorter production cycles urges for dedicated assessment and classification methods.

Using a photographic method followed by standardised computational algorithms is the way chosen to tackle this problem. The dimensions of the investigated samples allow to detect diffraction beams up to the second order which can be presented in a 5×5 matrix. An algorithm has to be able to convert digital images to equivalent intensity matrices and thereupon analyse their symmetry properties. On one hand, using chiral samples, obviously planar chirality should be measured, on the other hand rotational and mirror symmetries should be detected.

In order to tackle these different issues a package of computer programmes has been developed. The implemented process structure is sketched in Fig. 3.4 and detailed within the following sections.

Integration and preparation

An algorithm based on the programming language Perl[1] and the graphics library ImageMagick[2] has been developed to convert supplied Jpeg pictures of diffraction patterns into 5×5 intensity matrices. Diffraction patterns of regular square or rectangular arrays produce distinct and localised maxima. Given rough constraints—the number of diffraction orders and a rough estimate of the area they span over—the programme localises and logs their positions. Latter are estimated quite accurately using a method analogous to calculating a centre of mass.

The Jpeg image format created by the described setup encodes colors in 24 bit using the RGB scheme. This abbreviation relates to the three used base colours: red, green and blue. The He-Ne laser being a red light source, only information of the red channel with a remaining resolution of 8 bit equivalent to 256 levels can be processed. This reduced resolution excludes the possibility of direct use of intensity information like a maximum intensity because of unsatisfying

[1]For details see: `http://www.cpan.org/`
[2]For details see: `http://www.imagemagick.org/`

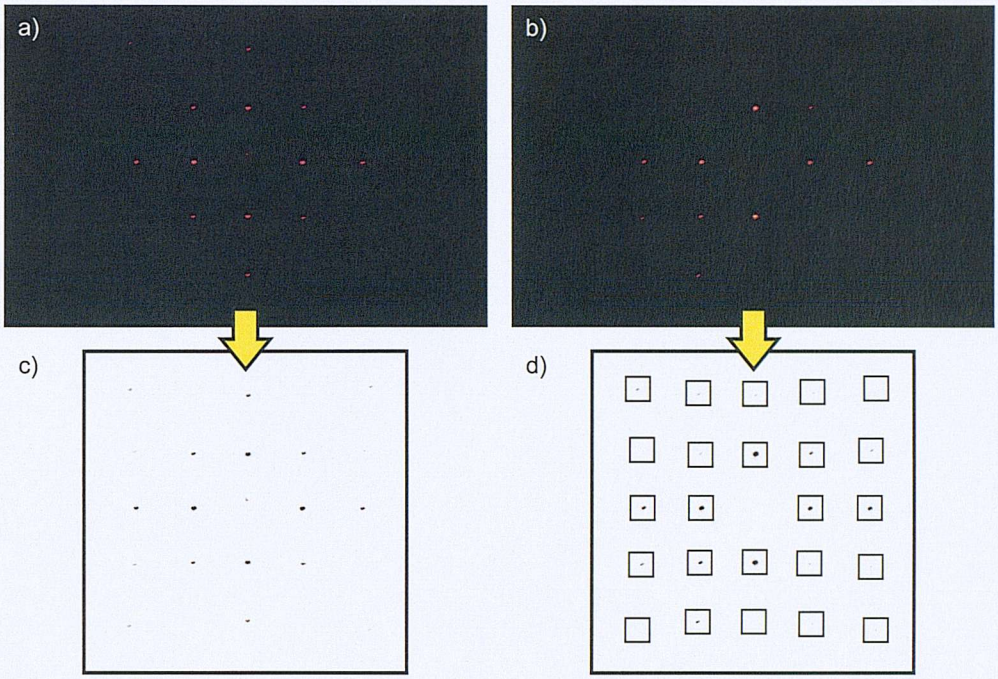

Figure 3.5: (a,b) Originally taken color images (a,b) first undergo (RGB) color separation: The inverted red channel is shown in grey-scale (c). Afterwards an integration process for each detected maximum initiates (d).

accuracy and comprehensiveness: The large anticipated intensity differences between the orders would lead to a considerable reduction of the amount of orders which can be observed and resolved simultaneously.

This problem can be solved by allowing the camera to saturate for intense diffraction orders and introducing integration methods: An intensity cross-section of a diffraction order is sketched in Fig. 3.6 a. Saturation and noise will distort the measurement and deform the obtained intensity distribution, compare part b. Two different methods have proven to be successful: Both integrate over a fixed area around the previously determined centre of the diffraction order and ignore all values below the noise level. Analysis of initial observations showed that the the noise was considerably smaller than 2% of the saturation level. The fixed noise threshold has consequently been set to

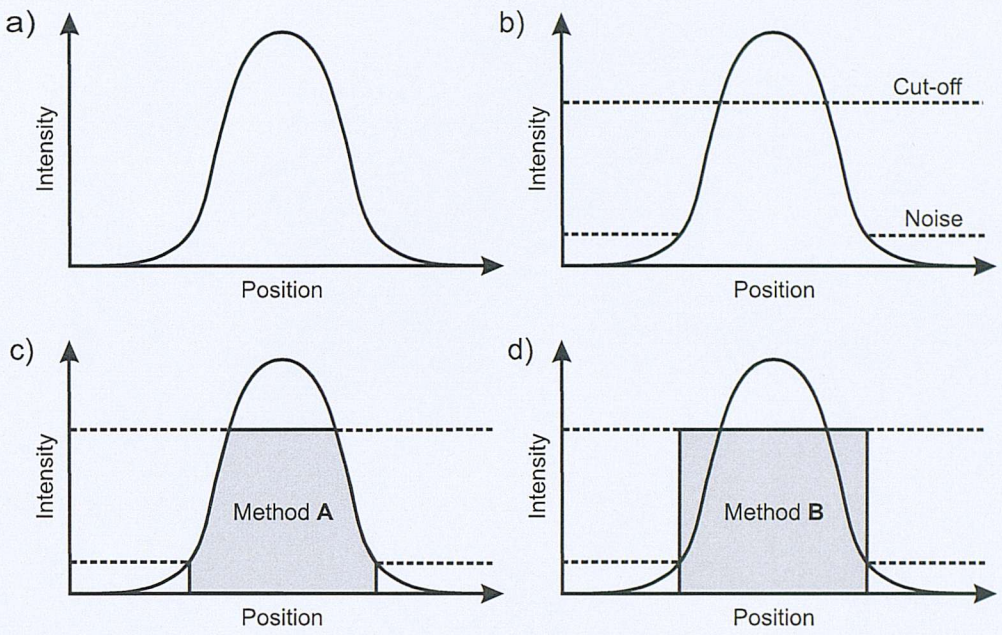

Figure 3.6: (a) A schematic cross-section through the intensity profile of a diffraction order is (b) deformed by the noise level and saturation of the detector. The picture *to* 5×5 matrix conversion algorithms use two different approaches both neglecting values below the noise level: (c) The obtained values are merely integrated by method **A**. (d) The noise level is used as a threshold to convert measurements into a $(0, 1)$ step-function which is thereupon integrated for method **B**.

an intensity of 6 compared to the maximum level of 255. Method **A** sums the intensity values within the depicted area, compare Fig. 3.6 c. Method **B** instead converts the intensity distribution to a (0,1) step-function assuming the value 'zero' below the noise level and 'one' elsewhere. A discussion of the applicability of these methods follows at a later stage alongside experimental results.

Correlation and symmetry analysis

Once an intensity matrix corresponding to a diffraction pattern has been created, an analysis of its symmetry can easily be performed using a well estab-

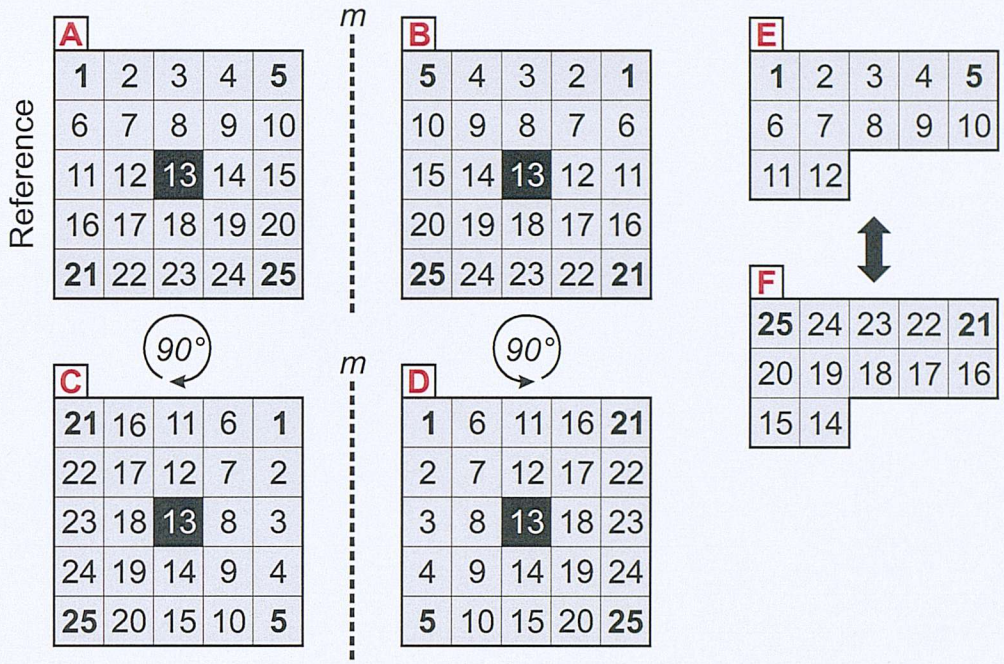

Figure 3.7: For a symmetry analysis using linear correlation the 5×5 intensity matrix of a diffraction pattern (**A**) has to be considered as a vector with 25 entries. In order to detect inherent symmetries it is compared to vectors of reordered matrices: The examples show the mirror image (**B**) along a line m, a rotation by 90° (**C**) and both operations performed after one another (**D**). A possible center of symmetry can be found even more easily by comparing the first half of matrix (**A**) shown as (**E**) with the last half in reverse order (**F**). For the case of comparing two matrices one has to identify the cases (**B**) to (**D**) with the ones corresponding to the second matrix. Of course a direct comparison with the unaltered second matrix can be performed additionally.

lished mathematical tool:

The linear correlation R of two sets of data $X = \{x_i\}$, $Y = \{y_i\}$, $i = 1 \ldots n$ is defined as

$$R_{XY} = \frac{E\left((X - \overline{x})(Y - \overline{y})\right)}{E\left((X - \overline{x})^2\right) \cdot E\left((Y - \overline{y})^2\right)} \tag{3.1}$$

where $E(\cdot)$ denotes expectancy and $\overline{x}, \overline{y}$ the arithmetic averages of the sets X, Y

(and vectors $\boldsymbol{x}, \boldsymbol{y}$ respectively) [Bronstein et al., 2000]. The correlation varies from -1 to 1, the latter indicating perfect correlation, zero no correlation.

In order to determine the symmetry of an intensity matrix its entries have to be reordered as a vector (x_i). The vector resulting of the transformed, e.g. rotated matrix (y_i) thereupon can be correlated to it[3]. The derived value measures the level of similarity of the matrices and vectors respectively, hence—in this case—the level with which a matrix displays the certain symmetry.

But moreover it is possible to compare observations, e.g. of two enantiomeric structures: By successively applying all conceivable symmetry operations to one of them followed by correlation to the unaltered other one, a transformation that might be linking the two cases can be found.

Inspired by microscopic observations of the structures, detailed in Sec. 3.2, the particular interests are whether the *fourfold symmetry* of the surface structure is inherited to the diffraction pattern and whether equal observations of enantiomers are mirror images of one another or more extraordianarily linked e.g. by an *anti-symmetry* [Shubnikov and Belov, 1964].

Programmes, again using the programming language Perl, have been written to perform the tasks of first of all comparing a matrix with itself after the application of various transformations. Secondly they are able to compare and judge the links between two arbitrarily different matrices. The used symmetry transformations are a 90°-rotation, reflection and the combination of the two. Additionally the quality of the centre of symmetry is established and the integration methods **A** and **B** described in the previous section are correlated. Figure 3.7 illustrates application and resulting reordering for all of these cases.

From statistics point of view correlation values have to be verified by determining their significance. While it has been excluded from the following discussion for lucidity, a t-test has been performed for all correlations and, where conclusions have been made, a sufficient significance has been reached—in many cases allowing a probability of non-validity of the zero hypothesis of lower than 0.001.

[3]Subsequent references to matrices shall likewise be seen as references to their vectors.

Chirality

Following correlation analysis the chirality displayed by the observations is evaluated. The discrete chirality measure κ which has been discussed earlier is used for this purpose. Instead of using the proposed chirality unit, within this section a near original definition of the measure will be employed [Potts et al., 2004, Eq. (17)]. It is defined by summing over all possible triangle combinations of a discretised object with their vertices being at $\boldsymbol{r}_i, \boldsymbol{r}_j, \boldsymbol{r}_k$ within the x, y-plane and corresponding masses of m_i, m_j, m_k as:

$$\kappa = \frac{1}{4} \sum_{i=1}^{N} \sum_{j=1}^{N} \sum_{k=1}^{N} m_i m_j m_k \frac{|\boldsymbol{r}_{ij}| - |\boldsymbol{r}_{ik}|}{|\boldsymbol{r}_{ij}| + |\boldsymbol{r}_{ik}|} (\boldsymbol{r}_{ij} \times \boldsymbol{r}_{ik}) \cdot \widehat{\boldsymbol{e}}_z \tag{3.2}$$

where $\boldsymbol{r}_{ij} = \boldsymbol{r}_j - \boldsymbol{r}_i$, $\boldsymbol{r}_{ik} = \boldsymbol{r}_k - \boldsymbol{r}_i$ and $\widehat{\boldsymbol{e}}_z$ is a normal vector in $+z$-direction.

Differences in absolute intensity for the investigated DPs resulted in the use of various exposure times with according relative intensities. This additional parameter is compensated for by normalisation: The intensity sum for each single matrix is integrated. As it corresponds to the mass term in Eq. (3.2) it can be used to normalise the chirality arriving at the following expression[4]:

$$\kappa_m = \frac{1}{4} \left(\sum_{i=1}^{N} m_i \right)^{-3} \sum_{i=1}^{N} \sum_{j=1}^{N} \sum_{k=1}^{N} m_i m_j m_k \frac{|\boldsymbol{r}_{ij}| - |\boldsymbol{r}_{ik}|}{|\boldsymbol{r}_{ij}| + |\boldsymbol{r}_{ik}|} (\boldsymbol{r}_{ij} \times \boldsymbol{r}_{ik}) \cdot \hat{\boldsymbol{e}}_z. \tag{3.3}$$

A Perl routine invokes a C++ programme for all acquired 5×5 matrices which successively applies this formula.

3.1.3 Results

Before a detailed consideration can be begun, several issues have to be resolved: Using the photographic method described above its equivalence to direct detector measurements has to be questioned. On one hand the saturation which is used deliberately might well change the relative intensity levels of the various diffracted orders, on the other the changes can be expected to be strictly

[4] A further discussion of mass-normalisation can be found in Sec. 2.1.4.

monotonous. Latter means that the symmetry and structure of the diffraction pattern ought to be retained which is found experimentally. Concerning the first question, correlation of detector to photographic data lead to values of about 0.75 indicating an agreement better than might be expected. More importantly however the symmetries found in the patterns exhibit themselves equally regardless of the adopted method.

Calculations made by Prof. S. Prosvirnin analogous to those used in Prosvirnin and Zheludev [2003] confirm the expectance of the centre of symmetry as the main symmetry ruling each DP. Since this constraint must be obeyed by any DP regardless of e.g. the polarisation configuration, it is also a measure of the quality for derived matrices. According to deliberations employed in Fig. 3.7 (case $\mathbf{E}\leftrightarrow\mathbf{F}$) linear correlation delivers values of more than 0.95 for all matrices that have been taken into consideration.

At the beginning two different integration methods have been suggested. In addition to all other calculations the matrices derived by those two methods have been correlated for each single diffraction pattern. Their near one correlation for the majority of all taken pictures (and particularly for all included in the following discussions) lets both methods appear equivalent and a further distinction between their results will not be made.

Stability measurements recording the DPs resulting from realignment of the 'crossed' analyser verified a stability of the pattern within at least $\pm 5°$. This is in agreement with expected conversion ratios resulting from azimuth rotation and ellipticity [Papakostas et al., 2003]. Furthermore, the fourfold rotational symmetry of the underlying 442 wallpaper group[5] gammadion pattern has been tested by rotating both polarisers in 90°-steps resulting into equivalent observations.

Fourfold symmetry

This fourfold rotational symmetry (C_4) should also establish itself within the diffraction pattern. For parallel polarisers this seems to be the case, see

[5] A very graphic introduction into wallpaper symmetries can be found in Ostromoukhov [1998] or at `http://xahlee.org/Wallpaper_dir/c5_17WallpaperGroups.html`.

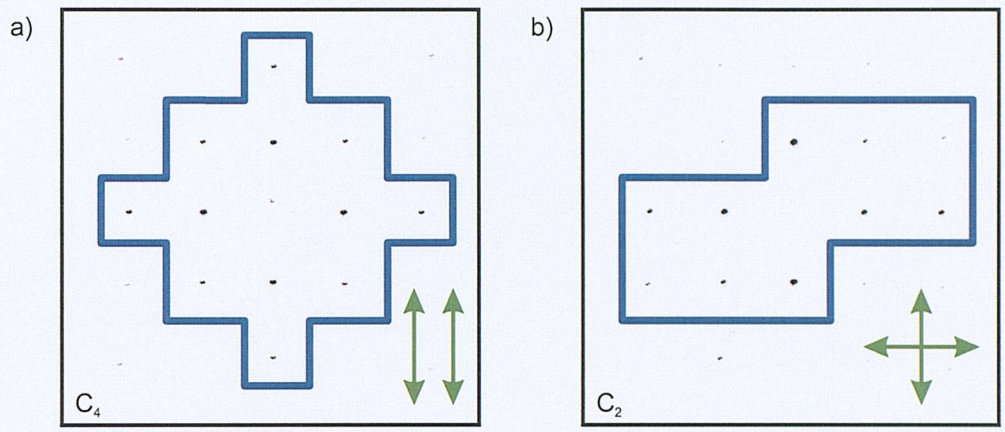

Figure 3.8: Symmetries of diffraction patterns of an open gammadion can be described by simple geometric structures (blue): (a) For parallel aligned polariser and analyser (green) the expected fourfold rotational symmetry (C_4) appears to be retained. (b) The contrast gained by crossing the polarisers reveals the actual twofold symmtetry (C_2).

Fig. 3.8 a. When however the analyser is oriented perpendicularly in respect to the initial polariser the gain in contrast reveals that the DP mereley retains a twofold symmetric structure, see Fig. 3.8 b.

This lower symmetry is imposed by the linear polarisation of the probing light and exposed in particular by the azimuth rotation capabilites of the PCS. Despite conventional wisdom that a grating symmetry directly determines the symmetry of its DP, it is shown that optically active planar materials can alter the symmetry. In this case not the chirality of the grid, but the chirality of the individual element is responsible for that change which is explained by Papakostas et al. [2003] and in addition motivated by the following.

Inherent chirality

It is possible to measure the chirality of a diffraction pattern. Yet their chiralities have to be normalised by intensity (and mass respectively) in order to diminish the influence of, on one hand, different exposure times used within the experiments and, on the other, discretisation effects for the calculated data.

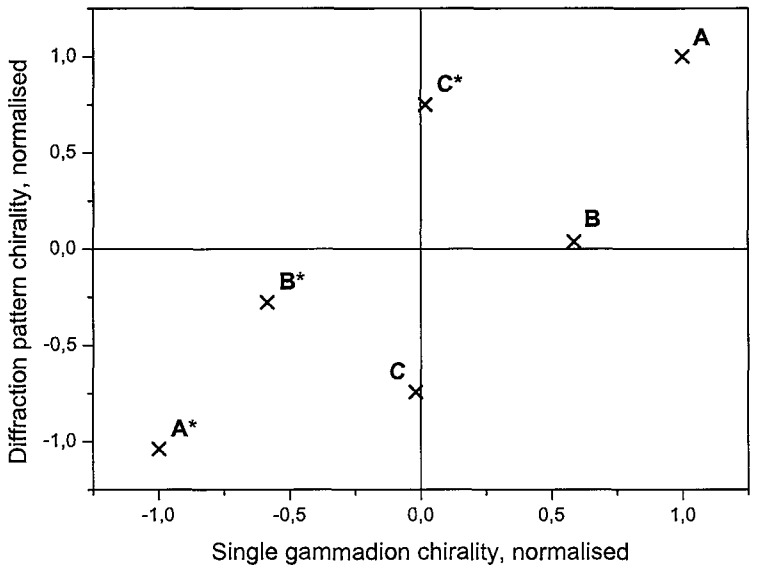

Figure 3.9: The chirality of diffraction patterns is qualitatively related to the chirality of the illuminated structure: Values for several gammadions (**A** – **C**) and their enantiomers (**A*** – **C***) are shown. Their bending angles are $\zeta_A = 45°$, $\zeta_B = 90°$ and $\zeta_C = 135°$, see Fig. 2.4 (p. 24). For both cases the chirality has been scaled arriving at a value of 1 for type **A**.

Furthermore, a value of 1 is assumed for the chirality displayed by an open gammadion ($\zeta = 45°$) to standardise the comparison.

The *S*-shaped structure of the cross-polarised DP in Fig. 3.8 b motivates a (clockwise) sense of twist. This term is closely related to chirality and how it is understood. All cross-polarised diffraction observations on PCS have shown to display chirality—yet to a very different extent depending on the type of gammadion.

The major expectation, enantiomeric sign reversal of the associated chirality is met and has been tested for various gammadion array types (bending angle, size, pitch) and experimental configurations (incident polarisation angle). This shows that the observed chiralities actually stem from the underlying PCS and not from any other influence.

The actual link between grid design and diffraction pattern however can

be created in a much more direct fashion: Figure 3.9 plots the chirality displayed by several diffraction patterns and compares them to the structural chirality that comes along with a single gammadion of the corresponding DP, cp. Fig. 2.9.

As only quadrants I and III of the coordinate system are populated, these chiralities strictly agree sign-wise. Yet they are clearly not on a line suggesting a qualitative, non-quantitative link. Interestingly the sign change for gammadions with large bending angles ($\zeta = 135°$) that the single gammadion chirality suggests is found in the DP. This is in contrast to the relation of gammadion chirality to azimuthal rotation of linearly polarised light described by Papakostas et al. [2003, Fig. 2 d] where this sign change had not been found.

The distinct differences between the chirality of a gammadion array to that of a single one, cp. Fig. 2.9 & 2.13, suggests that the observed interaction is dominated by the chirality and polarisation conversion capabilites of a single gammadion. This can be understood comparing the probing wavelength of 633 nm with the involved sizes within the array: It approximately equals the groove width and in contrast cannot span the distance between the grooves of two separate gammadions. This might of course be different for the case of sub-wavelength structures as used by Vallius et al. [2003].

The quantitative inconsistencies apparent in Fig. 3.9 can stem from various issues:

- Only up to second order beams have been taken into account using the 5×5 matrices. Bare eye observations of higher orders show that a considerable amount of the exhibited chirality of the overall pattern is observed for higher orders.

- The zero order beam has been blocked. Hence, the definition of the chirality measure employed implies all of the summed triangles involving this beam to be of zero value.

- This geometric chirality measure does not recognise chirality stemming from an unequal mass / intensity distribution within the vertices of a triangle in general. For the many isoscele or even equilateral triangles

linking these 25 orders it merely assumes a zero value while masses in two or more vertices differ, cp. Sec. 2.1.4.

- The chiralities had to be mass- / intensity-normalised in order to allow comparison. How sensitive this normalisation actually is, can be seen from examples discussed within the previous chapter. The conversion ratios of the different types of gammadions and hence the intensity detectable in cross-polarised configuration differ considerably, forcing to use significantly different exposure times.

- Finally, the manufacturing process involves a discretisation of the gammadion array, as well as the calculation of the single gammadion chirality does. Resulting relative changes stemming from differing thicknesses or slight disorientations might as well be responsible.

Nevertheless, opening a qualitative link between the chiralities of grid design and diffraction pattern has been successful.

Enantiomeric symmetry and time reversal

Comparison of cross-polarised DPs made of two enantiomers under equal conditions show that, despite the underlying arrays being mirror images of one another, their DPs are not (see Fig. 3.10 a/b). This condition is referred to as broken enantiomeric symmetry. Barron [1994] argues that enantiomeric time reversal—following the substitution by an enantiomer with time reversal—ought to be obeyed for chiral structures which in essence he relates to an overall ruling $\mathcal{CPT}$ symmetry. Yet if the enantiomeric symmetry $\mathcal{R}$ is violated, one can deduct that a time reversed $\mathcal{T}$ scenario must be broken as well to restore the overall postulated enantiomeric time reversal symmetry $\mathcal{RT}$ [Schwanecke et al., 2003].

In order to allow a number-wise verification of this visual analysis and further systematic investigation of various samples, the symmetries linking equal observations on enantiomeric gammadions have been compared, see Fig. 3.7. The symmetries equality, mirror image and 90°-rotation merely lead to correlations of less than 0.5. On the other hand, the comparison of a DP matrix with the

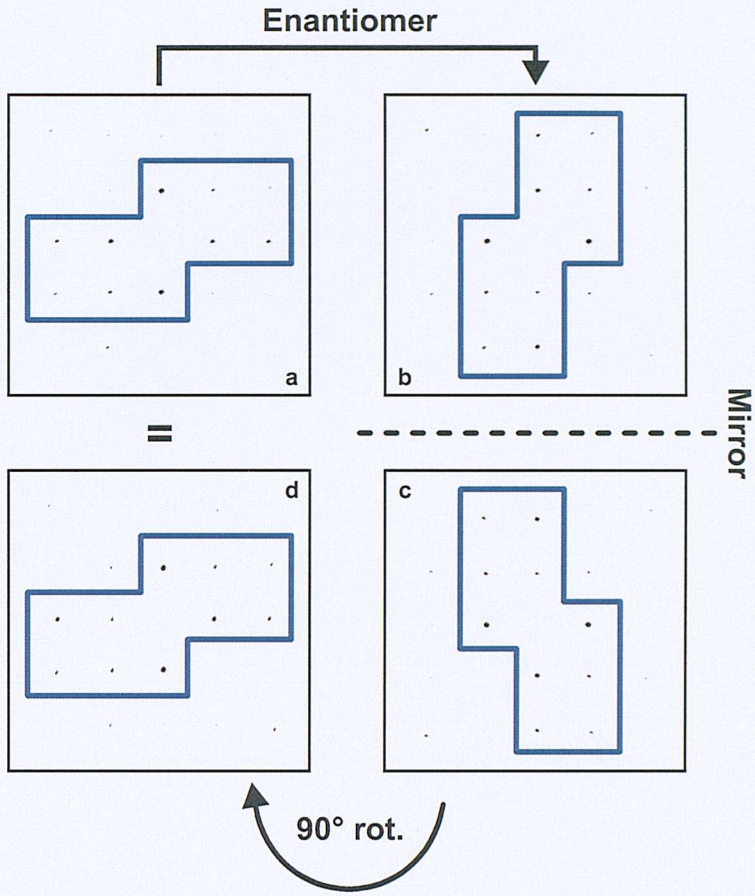

Figure 3.10: The cross-polarised diffraction pattern of an open gammadion (a) and its enantiomer (b) display similar intensity distributions. The mirror image (c) of the enantiomeric DP yet does not equal the original DP (a) resulting in broken *enantiomeric symmetry*. Subsequent 90°-rotation however yields equality (d).

mirror-imaged and 90°-rotated version of its enantiomer correlate with values greater than 0.94 for the open type of gammadion and holds nearly as well for other investigated PCSs. This symmetry has been applied to the visual example in Fig. 3.10, underpinning the numerical findings by receiving near-equality between parts a and d.

Overall, these considerations allow two striking conclusions: Despite the use of a mirror symmetric structure, the resulting field structure is not mirror

symmetric. This cannot be explained by an ordinary simplifying description like the interaction of a chiral structure with just the linear polarised electric field of the incident light wave. In contrast it has to be described by a more complex model referring to the complete triad $\boldsymbol{S} = \boldsymbol{E} \times \boldsymbol{H}$ of the wave. The involvement of the magnetic field and the possibility to obtain a DP equaling the initial case by following the mirror imaging of the enantiomeric DP with a 90°-rotation suggest to describe these findings in terms of black-and-white symmetry or Shubnikov anti-symmetry [Landau and Lifshitz, 1964; Shubnikov and Belov, 1964].

3.1.4 Conclusions

A semi-automated process structure involving several tools and allowing various kinds of symmetry analysis has been developed. It particularly enables and enhances future systematic investigations of arrays of PCS. Nevertheless, already several results have been gained by its application: Diffraction of linear polarised light on fourfold-rotational gammadion arrays displays only twofold-rotational patterns, which results from optical activity triggered by the chirality of the structure. These diffraction patterns themselves exhibit chirality which appears to be closely linked to the chirality of the base elements (gammadions) of the illuminated array. Observations of enantiomeric arrays show that they are actually not connected by the same enantiomeric transformation applied to the structure. They in contrast are equal only when applying a further 90°-rotation implying not only a violation of enantiomeric symmetry but also broken time reversal.

3.2 Polarisation sensitive microscopy

Some of the questions discussed in the previous section were motivated by an extensive preceding set of microscopic observations on various kinds of PCSs with a special focus on gammadion arrays. The main results that stimulated further investigations will be summarised in this section. Parts have been published in Schwanecke et al. [2003].

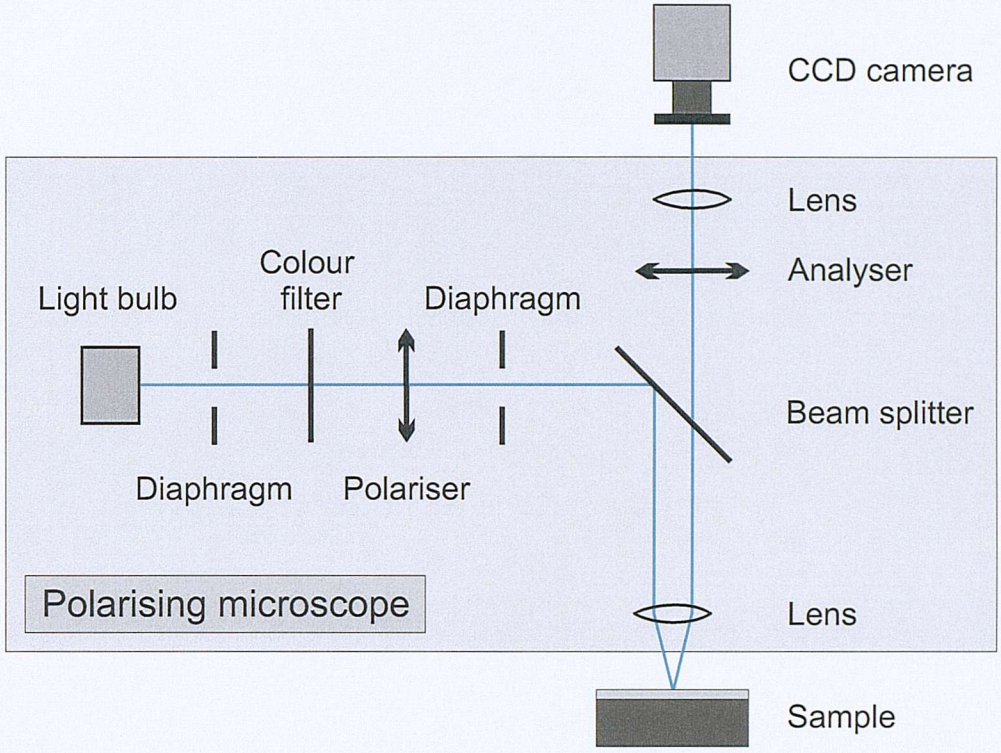

Figure 3.11: Experimental setup for the experiments involving the polarising microscope, further details can be found within the accompanying text.

3.2.1 Experimental setup

All data was gained using the polarising microscope Meiji ML 9400 and reflection mode illumination with a white light halogen source (Meiji MA 326 bulbs). The observations have as well been captured using a 6.3 megapixel low noise CMOS CCD camera (Canon EOS D60), mounted on the trinocular tube of the microscope, see Fig. 3.11. Apart from topographically motivated images the light incident was linear polarised and its electric field oriented horizontally in relation to the pictures displayed in this section (Fig. 3.12 b-d and 3.13 a/b). The reflected light was thereafter analysed using another linear polariser oriented perpendicularly in 'crossed' position. This particularly results in metallic regions appearing dark. Additionally, the involvement of

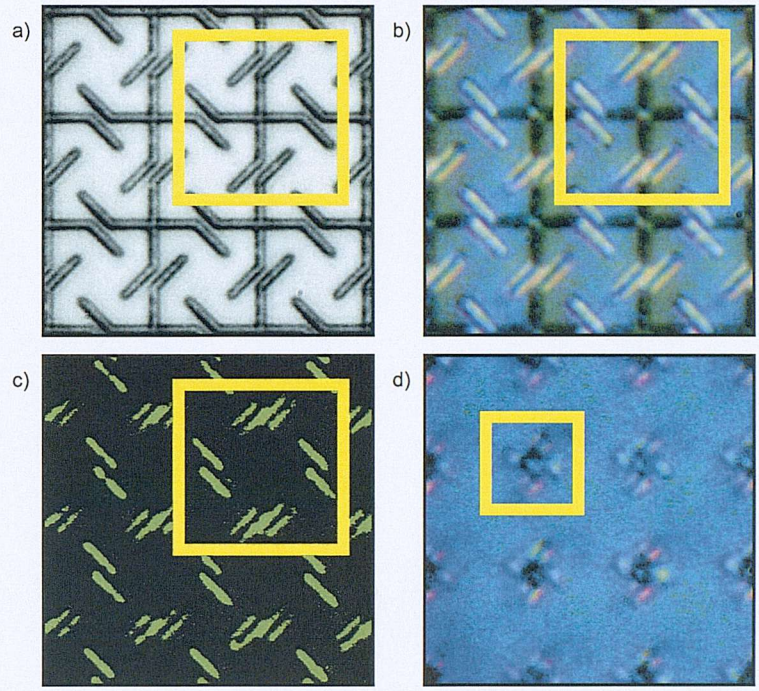

Figure 3.12: (a) The topography of an array of open gammadions (observed unpolarised) helps orientate within (b-d) cross-polarised observations. (b) External branches attached to the vertical or horizontal centre part appear coloured. The different types of response localising either near the walls (orange) or in the centre (blue) of the external gammadion branches are emphasized (c) in contrast-enhanced quasi-monochromatic observations at a wavelength of 530 nm, yielding multiple-bar structures. (d) These features are also seen for different gammadion sizes and pitches. Single gammadions are highlighted by a yellow box.

narrow-bandwidth spectral filters allowed quasi-monochromatic illumination which enhanced resolution and contrast considerably. A rotating table allowed to precisely control and alter the incident polarisation angle in respect to the structure. All photographs shown here have been taken using a 40× objective.

The gammadion arrays resemble those introduced in the previous chapter, but with slightly changed dimensions: The arm length l measures 4 μm (1.4 μm for Fig. 3.12 d) and the pitch 10 μm.

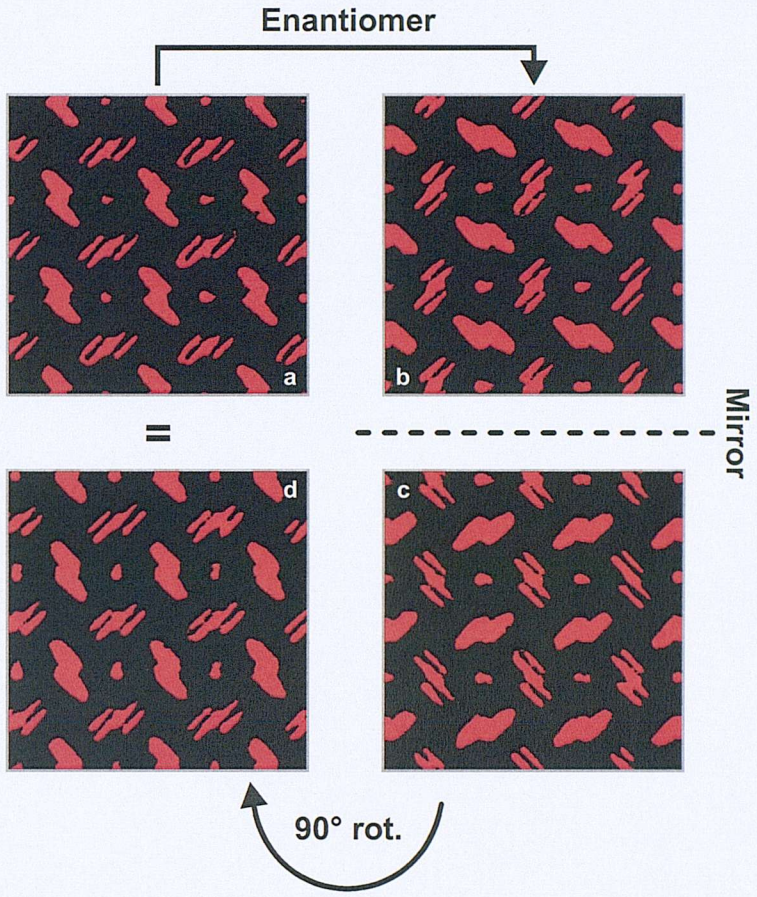

Figure 3.13: Contrast enhanced cross-polarised and quasi-monochromatic ($\lambda = 600\,\text{nm}$) observations of a gammadion array (a) and its enantiomer (b) are not mirror images of one another (c). However introducing an additionally applied 90°-rotation (d) reveals the link between the enantiomeric observations.

3.2.2 Results

The observations most noticeably show a colouring of branches oriented at 45° in respect to the electric field of the incident linear polarised light, see Fig. 3.12 b, d. This holds for several types of gammadions including those with bending angles ζ of $\pm 45°$, $\pm 90°$ and $\pm 135°$ and various sizes. The colourings destroy the fourfold symmetry that the original topography had shown

(Fig. 3.12 a). Further distinction is defined by differing localisation of the regions that appear to effectively reflect or re-emit the polarisation rotated light: Some branches appear bright in their centre while others have two bar-like bright zones next to the structure walls. Latter is emphasized for quasi-monochromatic illumination as seen in Fig. 3.12 c and 3.13.

Intriguingly the colouring differs between enantiomeric versions of gammadion arrays. The external branches connected to the vertical or horizontal centre part of the gammadion swap their appearance. This results in observations of two enantiomeric arrays not being mirror images of one another. Just as has been discussed in the section about diffraction patterns, this broken enantiomeric symmetry implicates a time non-reversal interaction. It appears to be the first report of this kind for non-magnetic materials which so far were believed to obey time-reversality. The introduction and imposition of the 2D chiral twist on the field structures might be understood as the anologon to the otherwise involved magnetic fields of the interacting substrate.

The observations are reproducible regardless of microscope magnification (40×, 10×, 4×), illumination area or observed part of the sample arrays. It is easily observable with a bare eye looking into the microscope and robust in respect to artificially introduced misalignments of the crossed polarisers for several degrees. Furthermore, rotation of the sample results in continuous fading of the previously coloured branches and expectedly restores every 90°.

3.2.3 Conclusions

Complementing the results of the diffraction experiments, microscopic imaging has been able to verify their results using a completely independent technique: The interconnected parts of the gammadion structure lead to different responses for branches connected to the central gammadion parts oriented parallel or perpendicularly in respect to the incident linear polarisation. The response is spectral dependent and shows two different localisation types. The broken fourfold symmetry furthermore violates the expected enantiomeric symmetry and resulted in the discovery of a time-nonreversal interaction.

3.3 Classification of galaxies

So far planar chirality has only been discussed in a context of optical interactions. On the other hand the introductory chapter already mentioned the plentiful appearance of the term chirality within many natural sciences. Here, an approach to apply the measure to galaxy classification will be presented. Galaxies are mostly categorised either by their spectrum or by their morphology. Latter involves various parameters—chirality often being explained alongside the terms of twist or spirality might become one of them.

3.3.1 Existing standards

The roots of nearly all major classification schemes go back to Hubble [1926, 1936] and try to relate to an underlying sequence of physical processes. Many major catalogues were classified by sighting. However even relying on experienced astronomers Naim et al. [1995] state that their classification of 831 galaxies using 6 independent researchers already introduces an uncertainty of 1.8 in units of the *Revised Hubble numerical index* T which users integers between -6 and 11 [de Vaucouleurs, 1959, 1963; de Vaucouleurs et al., 1991]. So there still is room for refinements or improvements applying rigorously defined rules and employing computational rather than human ressources.

The parameters that can be taken into consideration are numerous. Sandage [1975] provides a comprehensive overview of the main approaches. Examples of particular variables are ellipticity, the concentration of mass in the centre, the level to which spiral arms are developed (*luminosity classification*), etc. Naim et al. [1995] found that latter definition appears not to be well cut. As it refers to the spirality of a galaxy, it quite probably has a strong link to chirality.

Frequently cited catalogues like the *Third Reference Catalogue of Bright Galaxies* [de Vaucouleurs et al., 1991] and its predecessors or the *ESO catalogue* [Lauberts and Valentijn, 1989] contain several tens of thousands of classified galaxies. For more modern surveys spanning several tens of millions of galaxies the use of manpower in order to classify galaxies has reached its limit of feasibility. Many parameters are already mathematically well defined and modern image analysis methods will be able to distinguish between many of them. Yet

Figure 3.14: Several galaxies differing in spirality and chirality with their NGC numbers, taken from the catalogue by Naim et al. [1995].

the availability of a chirality measure which is integrable and fully scalable is only recent.

3.3.2 Implementation

This motivated the application of the programme suite introduced within the previous chapter. A catalogue of 113 nearby galaxies has been made freely available on the internet: `http://astro.princeton.edu/~frei/galaxy_catalog.html` by Frei et al. [1996]. It includes additional parameters like the revised Hubble numerical index and has been chosen as a starting point for a feasibility study. Before professional astronomers seriously can consider the use of this measure, it will have to be shown that the measurements

- are reproducable,
- converge within sensible time scales,
- agree sign-wise with the different senses of twist exhibited by spiral galaxies,
- are able to distinguish various levels of spirality significantly and
- can be normalised to allow different resolutions / obervation angles etc.

A method tackling part of latter issue has already been described in Sec. 2.2.2. As not only the size and resolution of CCD arrays used by astronomers but also

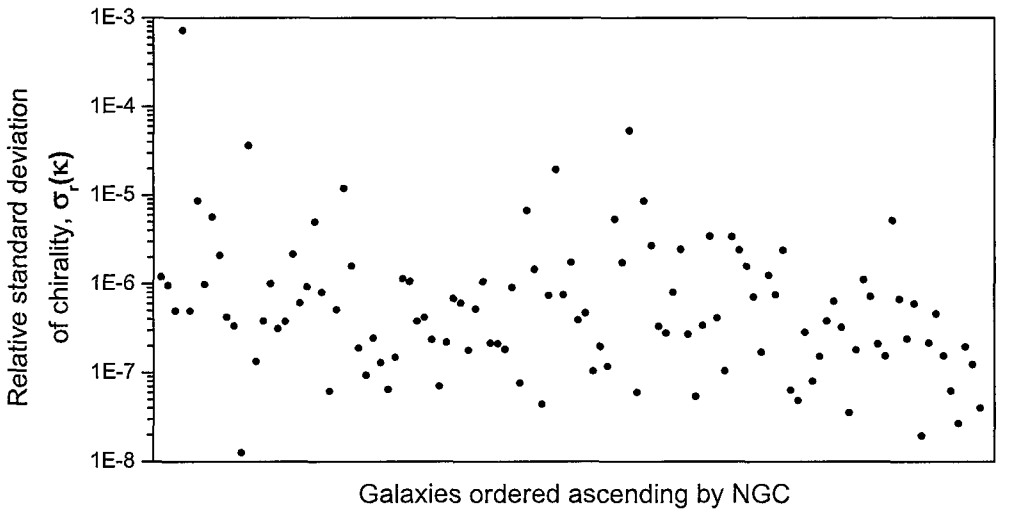

Figure 3.15: The relative standard deviation of the chirality approximations vary from galaxy to galaxy. The logarithmic plot against a list of the investigated galaxies, ordered by their NGC code, puts across the achieved level of accuracy.

observation angles and not least the distance, size and brightness of galaxies vary widely, their chirality must be free of these various influences. On one side is the area influence which for galaxies might best be described by an approximation of an elliptic area they occupy. An idea using a combination of linear fitting and assuming standard deviations relative to both axes has been chosen as reference for this section, see Fig. 2.3 and Sec. 2.2.2. This elliptic area normalised chirality will be noted κ_e in comparison to the conventional rectangular method noted κ_a.

The magnitude or brightness of a galaxy is another parameter to be separated from chirality. In an image further influences are exposure time and discretisation level. Hence, an approach similar to mass normalisation simply assuming an overall integrated intensity of $\sum_i m_i = 1$ for every galaxy as described in Sec. 2.1.4 can be employed. Together with the elliptitic area normalisation the fully normalised chirality measure will be denoted κ_{em}.

3.3.3 Results

In order to provide values that astronomers can use as a starting point for further investigation the complete catalogue by Frei et al. [1996] has been analysed. The chirality of many spiral galaxies can already be well established within 10^8 to 10^9 calculations which is a matter of minutes. Yet objects with small chirality like elliptical galaxies with marginal internal structure display a considerable reduced convergence speed. Three approximation sets with an overall total of 50 billion triangle calculations per galaxy are presented.

The obtained relative standard deviations $\sigma_r(\kappa)$ are depicted in Fig. 3.15. Nearly all galaxies reach levels where the obtained chirality can be considered reproducible. However, the question whether this value actually represents the accuracy of the measurements might arise. An answer is provided by Fig. 3.16. It provides a comparison between two scenarios each using a different selection of $2 \cdot 10^{10}$ randomised triangle calculations. While the standard deviation for scenario 2, $\sigma_r(\kappa_2)$, suggests accuracies between 10^{-4} and 10^{-8}, comparison of the independent scenarios supplies relative deviations, $(\kappa_2 - \kappa_1)/\kappa_2$, about 4 magnitudes higher. This effect has already been found for the calculations on artificial templates shown in the past chapter. There convergence was assumed for $\sigma_r(\kappa) \lessapprox 10^{-6}$. Here again this seems to correspond to an effective accuracy of about 10^{-2}.

This linear dependence between $\sigma_r(\kappa)$ and an effective accuracy can furthermore be affirmed by again employing linear correlation, see Sec. 3.1.2. The values for $\sigma_r(\kappa_2)$ and $(\kappa_2 - \kappa_1)/\kappa_2$ correlate with $R = 0.88$ which can be considered quite significant—non the least because the comparison is made in relation to the relative deviation $(\kappa_2 - \kappa_1)/\kappa_2$ where single values cannot necessarily be expected to be representative for the overall accuracy.

Accepting the accuracy of the calculations as sufficient, it is worthwhile to consider a couple of specific examples. For this purpose the intentionally very different galaxies of Fig. 3.14 will exemplify the application of the chirality measure. Figure 3.17 shows them in their grey-scaled version and ordered according to subjective perception of their twist: While NGC 3379 ($T = -5$) is very elliptical with next no substructure, NGC 3184 ($T = 6$) already con-

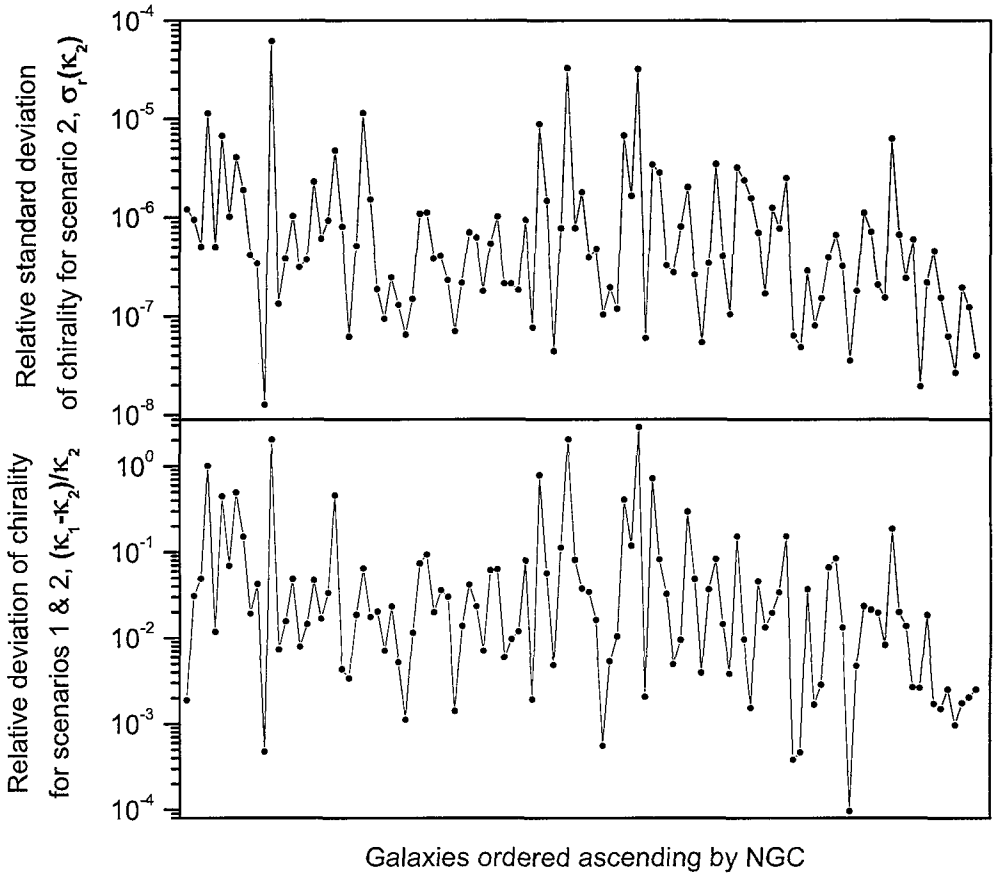

Figure 3.16: The relative standard deviation of one approximation correlates well with the relative deviation to another approximation ($R = 0.88$, see Eq. (3.1)). It however predicts an accuracy about 4 orders of magnitude too high.

tains developed spiral elements. Those are however embedded in a 'milky' disk structure and much clearer defined for NGC 4731 ($T = 6$).

One naturally would expect an increase of absolute chirality along these lines and is not let down by the calculation. Both κ_m and κ_{em} present sufficient resolution of about a magnitude. Furthermore, the obvious change of twist between NGC 3184 and NGC 4731 is reflected by the obtained chirality index. Typical for these Monte Carlo approximations again is that high chirality is accompanied by low relative standard deviation and vice versa. This constitutes

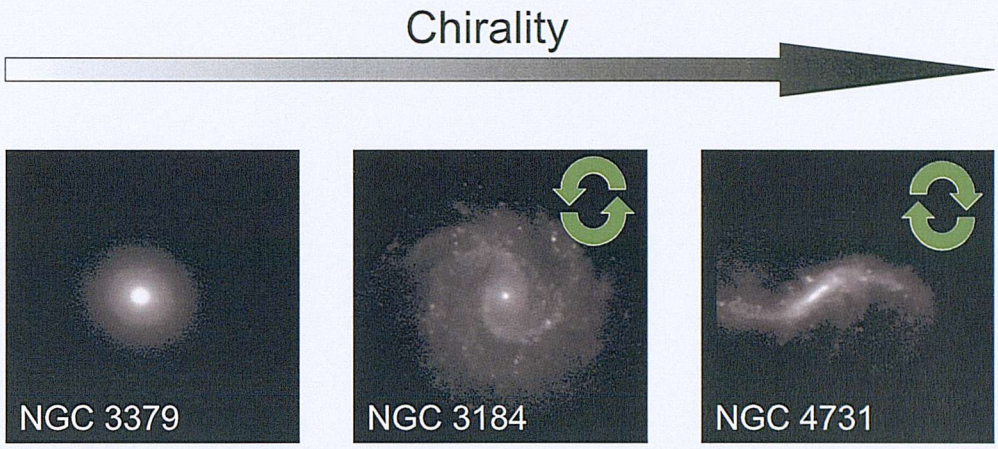

NGC	κ $[\hat{\kappa}]$	κ_m $[\hat{\kappa}]$	κ_{am} $[\hat{\kappa}]$	κ_{em} $[\hat{\kappa}]$	$\sigma_r(\kappa)$ [1]
3379	$5,41 \cdot 10^{14}$	$7,44 \cdot 10^{-4}$	$8,19 \cdot 10^{-9}$	$3,66 \cdot 10^{-7}$	$5,02 \cdot 10^{-6}$
3184	$-2,74 \cdot 10^{17}$	$-1,83 \cdot 10^{-2}$	$-1,87 \cdot 10^{-7}$	$-2,92 \cdot 10^{-6}$	$3,82 \cdot 10^{-7}$
4731	$3,45 \cdot 10^{17}$	$1,86 \cdot 10^{-1}$	$2,23 \cdot 10^{-6}$	$4,67 \cdot 10^{-5}$	$6,39 \cdot 10^{-8}$

Figure 3.17: The automatically converted grey-scale counterparts of Fig. 3.14 diplay the expected chirality characteristics—namely an increase of chirality according to the ordering and opposite sign for the two spiral galaxies.

another indication why a limit for the maximum number of calculations should be included in any chirality approximation algorithm.

An attempt to plot chirality against the revised Hubble numerical index shows some structure, see Fig. 3.18. Yet the small amount of galaxies and the involvement of so many other paramaters into the determination of the T value do not allow to conclude direct interconnections. Ignoring exotic galaxies at the end of the scale, the falling average for elliptic galaxies ($-3 \leq T \leq 0$) and the threefold increase for spiral galaxies ($1 \leq T \leq 9$) attract attention. A detailed interpretation however has to be left to a professional astronomer. The corresponding numerical values can be found in Tab. 3.2. It should be noted that the standard deviation assumed as the error might not be appropriate for the probably not normal but χ^2-distributed values of $|\kappa_{em}| \geq 0$. Still the most

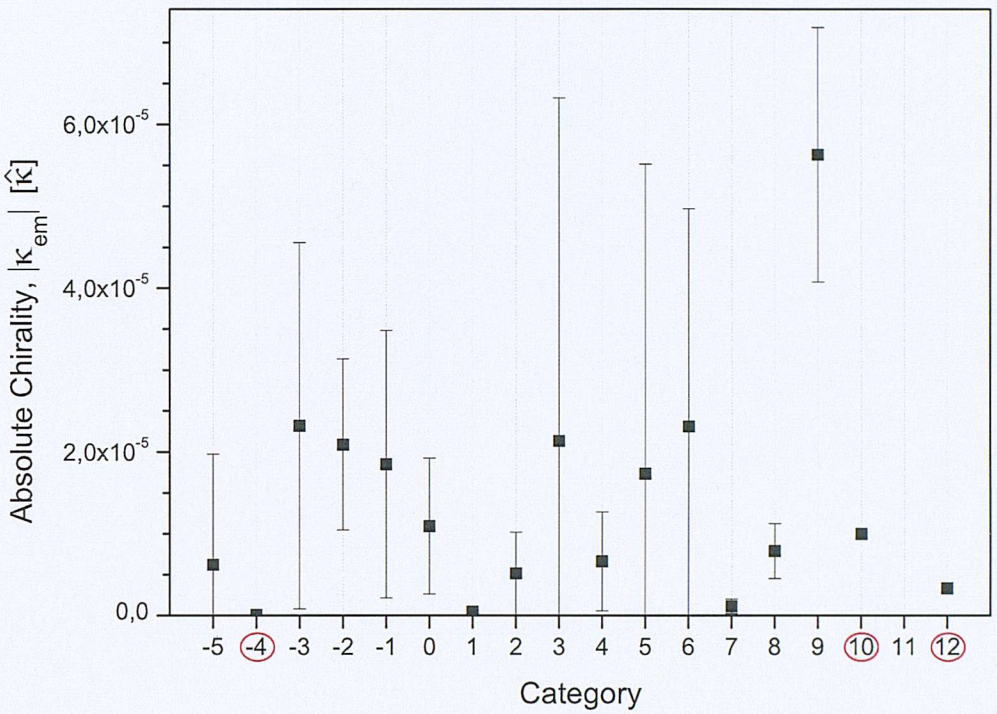

Figure 3.18: Absolute chiralities with their standards deviations are compared to the revised Hubble numerical index, see also Tab. 3.2. Where only one galaxy is available, the index has been circled red.

important follow-up measure will have to be to tackle even larger catalogues involving more galaxies per category and respecting the other categorisation parameters.

Another interesting option for the renormalisation of the chirality index, which might improve the explanatory power of galaxy chirality, might be gained when bearing in mind their relative tilt in respect to our direction of observation. The newly introduced concept of an area-normal and its projection against the observation direction (Sec. 2.1.2) allows to recalculate the chirality which in first instance always is a virtual one. Respecting the influence of the observation angle the theory hence allows directly and without any application of further concepts to calculate a general measure of the chirality and spirality respectively of a galaxy. According data for the investigated galaxies however

T	n	$\lvert\kappa\rvert$ $[\hat{\kappa}]$	$\sigma_r(\lvert\kappa\rvert)$	$\lvert\kappa_m\rvert$ $[\hat{\kappa}]$	$\sigma_r(\lvert\kappa_m\rvert)$	$\lvert\kappa_{em}\rvert$ $[\hat{\kappa}]$	$\sigma_r(\lvert\kappa_{em}\rvert)$
−5	13	$1,49 \cdot 10^{16}$	1,33	$1,51 \cdot 10^{-2}$	1,81	$6,22 \cdot 10^{-6}$	2,17
−4	1	$5,41 \cdot 10^{15}$	–	$3,13 \cdot 10^{-4}$	–	$7,19 \cdot 10^{-8}$	–
−3	2	$5,56 \cdot 10^{16}$	0,98	$9,41 \cdot 10^{-2}$	0,98	$2,32 \cdot 10^{-5}$	0,97
−2	2	$9,59 \cdot 10^{16}$	0,65	$7,00 \cdot 10^{-2}$	0,48	$2,09 \cdot 10^{-5}$	0,50
−1	4	$3,08 \cdot 10^{16}$	1,03	$3,49 \cdot 10^{-2}$	0,82	$1,85 \cdot 10^{-5}$	0,88
0	2	$4,37 \cdot 10^{16}$	0,14	$4,00 \cdot 10^{-2}$	0,71	$1,09 \cdot 10^{-5}$	0,76
1	3	$2,01 \cdot 10^{16}$	1,12	$2,28 \cdot 10^{-3}$	0,54	$4,44 \cdot 10^{-7}$	0,50
2	9	$2,11 \cdot 10^{20}$	2,73	$7,19 \cdot 10^{-2}$	1,24	$5,15 \cdot 10^{-6}$	0,98
3	14	$3,33 \cdot 10^{18}$	1,99	$1,47 \cdot 10^{-1}$	1,94	$2,13 \cdot 10^{-5}$	1,96
4	17	$2,41 \cdot 10^{20}$	3,57	$1,04 \cdot 10^{-1}$	2,04	$6,63 \cdot 10^{-6}$	0,91
5	22	$1,13 \cdot 10^{18}$	2,03	$9,93 \cdot 10^{-2}$	2,65	$1,73 \cdot 10^{-5}$	2,17
6	15	$3,96 \cdot 10^{18}$	1,99	$1,31 \cdot 10^{-1}$	1,04	$2,31 \cdot 10^{-5}$	1,15
7	3	$3,89 \cdot 10^{16}$	1,14	$6,19 \cdot 10^{-3}$	0,72	$1,13 \cdot 10^{-6}$	0,79
8	2	$4,33 \cdot 10^{17}$	0,84	$4,78 \cdot 10^{-2}$	0,30	$7,89 \cdot 10^{-6}$	0,43
9	2	$2,24 \cdot 10^{17}$	0,28	$2,54 \cdot 10^{-1}$	0,34	$5,63 \cdot 10^{-5}$	0,28
10	1	$6,74 \cdot 10^{17}$	–	$4,30 \cdot 10^{-2}$	–	$9,96 \cdot 10^{-6}$	–
12	1	$3,96 \cdot 10^{17}$	–	$1,70 \cdot 10^{-2}$	–	$3,33 \cdot 10^{-6}$	–

Table 3.2: Absolute chiralities are compared to the revised Hubble numerical index, see also Fig. 3.18. Additionally the number of available galaxies per category n is noted. The normalised κ_e and κ_{em} display significantly lower standard deviation for most categories than κ itself.

has not been available.

3.3.4 Conclusions

It has generally been shown that the chirality measure in combination with the Monte Carlo method is a viable image analysis method. Furthermore it is capable of distinguishing the spirality of galaxies. The combination with normalisation (area, intensity) and re-normalisation (observation angle) techniques enhances its applicability for images of arbitrary format. All major initially set up demands have been met (p. 63). While templates in the previous chapter have not always used the full capabilities of the Monte Carlo method, the number of triangle calculations employed here stays up to eight magnitudes lower than what direct calculation would require.

While some structure has been seen for comparison with the revised Hubble numerical index a dedicated analysis including the other parameters defining the index has to be conducted on preferably larger catalogues. However already values for 113 different galaxies have been made available for further studies by astronomers.

3.3.5 List of investigated galaxies

Table 3.3: Comprehensive summary of chiralities for all investigated galaxies.

NGC	κ $[\hat{\kappa}]$	κ_m $[\hat{\kappa}]$	κ_{am} $[\hat{\kappa}]$	κ_{em} $[\hat{\kappa}]$	$\sigma_r(\kappa)$ [1]
2403	$-2,68 \cdot 10^{19}$	$-3,91 \cdot 10^{-2}$	$-7,53 \cdot 10^{-8}$	$-1,70 \cdot 10^{-6}$	$1,21 \cdot 10^{-6}$
2541	$1,89 \cdot 10^{17}$	$4,10 \cdot 10^{-2}$	$2,55 \cdot 10^{-7}$	$3,01 \cdot 10^{-6}$	$9,68 \cdot 10^{-7}$
2683	$-1,92 \cdot 10^{17}$	$-1,76 \cdot 10^{-2}$	$-1,81 \cdot 10^{-7}$	$-5,25 \cdot 10^{-6}$	$4,96 \cdot 10^{-7}$
2715	$4,61 \cdot 10^{14}$	$4,23 \cdot 10^{-4}$	$4,83 \cdot 10^{-9}$	$1,46 \cdot 10^{-7}$	$7,28 \cdot 10^{-4}$
2768	$6,11 \cdot 10^{16}$	$1,51 \cdot 10^{-2}$	$1,55 \cdot 10^{-7}$	$4,40 \cdot 10^{-6}$	$4,96 \cdot 10^{-7}$
2775	$3,21 \cdot 10^{15}$	$7,98 \cdot 10^{-4}$	$8,20 \cdot 10^{-9}$	$2,09 \cdot 10^{-7}$	$8,69 \cdot 10^{-6}$
2903	$6,14 \cdot 10^{19}$	$7,87 \cdot 10^{-2}$	$1,51 \cdot 10^{-7}$	$2,07 \cdot 10^{-6}$	$9,90 \cdot 10^{-7}$
2976	$4,74 \cdot 10^{15}$	$9,92 \cdot 10^{-4}$	$1,60 \cdot 10^{-8}$	$3,31 \cdot 10^{-7}$	$5,70 \cdot 10^{-6}$
2985	$-3,16 \cdot 10^{15}$	$-3,46 \cdot 10^{-3}$	$-3,74 \cdot 10^{-8}$	$-9,06 \cdot 10^{-7}$	$2,11 \cdot 10^{-6}$
3031	$-1,84 \cdot 10^{21}$	$-1,05 \cdot 10^{-1}$	$-2,01 \cdot 10^{-7}$	$-2,81 \cdot 10^{-6}$	$4,24 \cdot 10^{-7}$
3077	$3,98 \cdot 10^{17}$	$1,70 \cdot 10^{-2}$	$1,74 \cdot 10^{-7}$	$3,33 \cdot 10^{-6}$	$3,37 \cdot 10^{-7}$
3079	$6,73 \cdot 10^{18}$	$1,28 \cdot 10^{0}$	$1,30 \cdot 10^{-5}$	$1,76 \cdot 10^{-4}$	$1,27 \cdot 10^{-8}$
3147	$1,01 \cdot 10^{14}$	$1,33 \cdot 10^{-4}$	$1,51 \cdot 10^{-9}$	$3,13 \cdot 10^{-8}$	$3,65 \cdot 10^{-5}$
3166	$-3,74 \cdot 10^{16}$	$-6,81 \cdot 10^{-2}$	$-7,00 \cdot 10^{-7}$	$-1,92 \cdot 10^{-5}$	$1,35 \cdot 10^{-7}$
3184	$-2,74 \cdot 10^{17}$	$-1,83 \cdot 10^{-2}$	$-1,87 \cdot 10^{-7}$	$-2,92 \cdot 10^{-6}$	$3,82 \cdot 10^{-7}$
3198	$-6,13 \cdot 10^{17}$	$-2,38 \cdot 10^{-2}$	$-1,48 \cdot 10^{-7}$	$-2,00 \cdot 10^{-6}$	$1,01 \cdot 10^{-6}$
3319	$-1,35 \cdot 10^{18}$	$-7,88 \cdot 10^{-2}$	$-4,90 \cdot 10^{-7}$	$-5,45 \cdot 10^{-6}$	$3,14 \cdot 10^{-7}$
3344	$-1,96 \cdot 10^{17}$	$-1,34 \cdot 10^{-2}$	$-1,87 \cdot 10^{-7}$	$-3,08 \cdot 10^{-6}$	$3,79 \cdot 10^{-7}$
3351	$-5,91 \cdot 10^{16}$	$-2,47 \cdot 10^{-3}$	$-2,60 \cdot 10^{-8}$	$-4,99 \cdot 10^{-7}$	$2,16 \cdot 10^{-6}$
3368	$-1,55 \cdot 10^{17}$	$-1,30 \cdot 10^{-2}$	$-1,33 \cdot 10^{-7}$	$-2,76 \cdot 10^{-6}$	$6,11 \cdot 10^{-7}$

Table 3.3: Comprehensive summary of chiralities ... (continued)

NGC	κ $[\hat{\kappa}]$	κ_m $[\hat{\kappa}]$	κ_{am} $[\hat{\kappa}]$	κ_{em} $[\hat{\kappa}]$	$\sigma_r(\kappa)$ [1]
3377	$9,34 \cdot 10^{14}$	$4,54 \cdot 10^{-3}$	$4,79 \cdot 10^{-8}$	$2,13 \cdot 10^{-6}$	$9,27 \cdot 10^{-7}$
3379	$5,41 \cdot 10^{14}$	$7,44 \cdot 10^{-4}$	$8,19 \cdot 10^{-9}$	$3,66 \cdot 10^{-7}$	$5,02 \cdot 10^{-6}$
3486	$-1,79 \cdot 10^{16}$	$-7,11 \cdot 10^{-3}$	$-7,30 \cdot 10^{-8}$	$-2,04 \cdot 10^{-6}$	$8,08 \cdot 10^{-7}$
3556	$5,26 \cdot 10^{17}$	$7,59 \cdot 10^{-2}$	$2,10 \cdot 10^{-6}$	$3,44 \cdot 10^{-5}$	$6,24 \cdot 10^{-8}$
3596	$1,08 \cdot 10^{16}$	$1,22 \cdot 10^{-2}$	$1,26 \cdot 10^{-7}$	$4,40 \cdot 10^{-6}$	$5,14 \cdot 10^{-7}$
3623	$7,83 \cdot 10^{15}$	$6,91 \cdot 10^{-4}$	$7,08 \cdot 10^{-9}$	$1,34 \cdot 10^{-7}$	$1,20 \cdot 10^{-5}$
3631	$-7,53 \cdot 10^{15}$	$-2,14 \cdot 10^{-3}$	$-2,73 \cdot 10^{-8}$	$-7,84 \cdot 10^{-7}$	$1,60 \cdot 10^{-6}$
3672	$-7,93 \cdot 10^{16}$	$-5,54 \cdot 10^{-2}$	$-5,70 \cdot 10^{-7}$	$-1,56 \cdot 10^{-5}$	$1,90 \cdot 10^{-7}$
3675	$2,64 \cdot 10^{17}$	$8,51 \cdot 10^{-2}$	$8,69 \cdot 10^{-7}$	$1,98 \cdot 10^{-5}$	$9,40 \cdot 10^{-8}$
3726	$-9,63 \cdot 10^{16}$	$-2,52 \cdot 10^{-2}$	$-2,64 \cdot 10^{-7}$	$-6,74 \cdot 10^{-6}$	$2,45 \cdot 10^{-7}$
3810	$2,34 \cdot 10^{17}$	$6,32 \cdot 10^{-2}$	$6,49 \cdot 10^{-7}$	$1,90 \cdot 10^{-5}$	$1,30 \cdot 10^{-7}$
3877	$-3,87 \cdot 10^{17}$	$-2,53 \cdot 10^{-1}$	$-2,60 \cdot 10^{-6}$	$-6,96 \cdot 10^{-5}$	$6,50 \cdot 10^{-8}$
3893	$-5,21 \cdot 10^{16}$	$-2,96 \cdot 10^{-2}$	$-3,06 \cdot 10^{-7}$	$-1,29 \cdot 10^{-5}$	$1,49 \cdot 10^{-7}$
3938	$9,02 \cdot 10^{16}$	$5,14 \cdot 10^{-3}$	$5,31 \cdot 10^{-8}$	$1,23 \cdot 10^{-6}$	$1,14 \cdot 10^{-6}$
3953	$2,41 \cdot 10^{16}$	$3,89 \cdot 10^{-3}$	$3,99 \cdot 10^{-8}$	$1,06 \cdot 10^{-6}$	$1,07 \cdot 10^{-6}$
4013	$5,75 \cdot 10^{15}$	$5,50 \cdot 10^{-2}$	$5,61 \cdot 10^{-7}$	$9,63 \cdot 10^{-6}$	$3,79 \cdot 10^{-7}$
4030	$6,66 \cdot 10^{16}$	$1,70 \cdot 10^{-2}$	$1,74 \cdot 10^{-7}$	$5,32 \cdot 10^{-6}$	$4,19 \cdot 10^{-7}$
4088	$2,30 \cdot 10^{17}$	$4,93 \cdot 10^{-2}$	$5,07 \cdot 10^{-7}$	$1,67 \cdot 10^{-5}$	$2,36 \cdot 10^{-7}$
4123	$-2,01 \cdot 10^{16}$	$-4,44 \cdot 10^{-2}$	$-4,56 \cdot 10^{-7}$	$-2,48 \cdot 10^{-5}$	$7,07 \cdot 10^{-8}$
4125	$-8,19 \cdot 10^{15}$	$-2,48 \cdot 10^{-2}$	$-2,61 \cdot 10^{-7}$	$-9,34 \cdot 10^{-6}$	$2,20 \cdot 10^{-7}$
4136	$-1,48 \cdot 10^{16}$	$-9,21 \cdot 10^{-3}$	$-9,46 \cdot 10^{-8}$	$-2,97 \cdot 10^{-6}$	$6,84 \cdot 10^{-7}$
4144	$-2,88 \cdot 10^{16}$	$-2,15 \cdot 10^{-2}$	$-2,20 \cdot 10^{-7}$	$-6,19 \cdot 10^{-6}$	$6,13 \cdot 10^{-7}$
4157	$2,96 \cdot 10^{16}$	$1,28 \cdot 10^{-1}$	$1,31 \cdot 10^{-6}$	$2,42 \cdot 10^{-5}$	$1,80 \cdot 10^{-7}$
4178	$-7,97 \cdot 10^{17}$	$-6,22 \cdot 10^{-2}$	$-3,87 \cdot 10^{-7}$	$-4,52 \cdot 10^{-6}$	$5,21 \cdot 10^{-7}$
4189	$3,49 \cdot 10^{16}$	$1,76 \cdot 10^{-2}$	$1,71 \cdot 10^{-7}$	$2,01 \cdot 10^{-6}$	$1,06 \cdot 10^{-6}$
4192	$3,02 \cdot 10^{19}$	$2,91 \cdot 10^{-1}$	$9,26 \cdot 10^{-7}$	$1,20 \cdot 10^{-5}$	$2,15 \cdot 10^{-7}$
4216	$-2,45 \cdot 10^{19}$	$-3,45 \cdot 10^{-1}$	$-1,10 \cdot 10^{-6}$	$-1,44 \cdot 10^{-5}$	$2,12 \cdot 10^{-7}$
4242	$6,73 \cdot 10^{16}$	$3,32 \cdot 10^{-2}$	$3,74 \cdot 10^{-7}$	$1,12 \cdot 10^{-5}$	$1,83 \cdot 10^{-7}$

Table 3.3: Comprehensive summary of chiralities ... (continued)

NGC	κ $[\hat{\kappa}]$	κ_m $[\hat{\kappa}]$	κ_{am} $[\hat{\kappa}]$	κ_{em} $[\hat{\kappa}]$	$\sigma_r(\kappa)$ [1]
4254	$-1,48 \cdot 10^{18}$	$-1,93 \cdot 10^{-2}$	$-1,21 \cdot 10^{-7}$	$-2,13 \cdot 10^{-6}$	$9,10 \cdot 10^{-7}$
4258	$3,68 \cdot 10^{21}$	$9,12 \cdot 10^{-1}$	$1,75 \cdot 10^{-6}$	$2,21 \cdot 10^{-5}$	$7,68 \cdot 10^{-8}$
4303	$1,02 \cdot 10^{18}$	$6,71 \cdot 10^{-3}$	$2,13 \cdot 10^{-8}$	$3,43 \cdot 10^{-7}$	$6,73 \cdot 10^{-6}$
4321	$-3,56 \cdot 10^{19}$	$-4,96 \cdot 10^{-2}$	$-9,53 \cdot 10^{-8}$	$-1,32 \cdot 10^{-6}$	$1,46 \cdot 10^{-6}$
4340	$1,13 \cdot 10^{16}$	$8,43 \cdot 10^{-2}$	$8,80 \cdot 10^{-7}$	$4,52 \cdot 10^{-5}$	$4,42 \cdot 10^{-8}$
4365	$5,67 \cdot 10^{16}$	$1,10 \cdot 10^{-2}$	$1,13 \cdot 10^{-7}$	$2,33 \cdot 10^{-6}$	$7,42 \cdot 10^{-7}$
4374	$5,63 \cdot 10^{14}$	$3,09 \cdot 10^{-4}$	$3,21 \cdot 10^{-9}$	$1,09 \cdot 10^{-7}$	$1,96 \cdot 10^{-5}$
4394	$-1,15 \cdot 10^{17}$	$-1,64 \cdot 10^{-2}$	$-1,59 \cdot 10^{-7}$	$-2,36 \cdot 10^{-6}$	$7,54 \cdot 10^{-7}$
4406	$-1,63 \cdot 10^{16}$	$-4,00 \cdot 10^{-3}$	$-4,08 \cdot 10^{-8}$	$-1,03 \cdot 10^{-6}$	$1,75 \cdot 10^{-6}$
4414	$1,39 \cdot 10^{18}$	$5,62 \cdot 10^{-2}$	$3,50 \cdot 10^{-7}$	$5,28 \cdot 10^{-6}$	$3,92 \cdot 10^{-7}$
4429	$8,30 \cdot 10^{16}$	$1,95 \cdot 10^{-2}$	$2,01 \cdot 10^{-7}$	$5,14 \cdot 10^{-6}$	$4,71 \cdot 10^{-7}$
4442	$3,36 \cdot 10^{16}$	$1,04 \cdot 10^{-1}$	$1,07 \cdot 10^{-6}$	$3,13 \cdot 10^{-5}$	$1,04 \cdot 10^{-7}$
4449	$-6,75 \cdot 10^{17}$	$-4,29 \cdot 10^{-2}$	$-4,41 \cdot 10^{-7}$	$-9,96 \cdot 10^{-6}$	$1,98 \cdot 10^{-7}$
4450	$2,63 \cdot 10^{17}$	$6,12 \cdot 10^{-2}$	$6,26 \cdot 10^{-7}$	$1,56 \cdot 10^{-5}$	$1,18 \cdot 10^{-7}$
4472	$1,08 \cdot 10^{16}$	$8,96 \cdot 10^{-4}$	$1,07 \cdot 10^{-8}$	$2,25 \cdot 10^{-7}$	$5,38 \cdot 10^{-6}$
4477	$8,94 \cdot 10^{14}$	$1,44 \cdot 10^{-3}$	$1,47 \cdot 10^{-8}$	$8,10 \cdot 10^{-7}$	$1,74 \cdot 10^{-6}$
4486	$-5,39 \cdot 10^{15}$	$-3,13 \cdot 10^{-4}$	$-3,31 \cdot 10^{-9}$	$-7,18 \cdot 10^{-8}$	$5,37 \cdot 10^{-5}$
4487	$1,99 \cdot 10^{17}$	$1,92 \cdot 10^{-1}$	$1,96 \cdot 10^{-6}$	$3,96 \cdot 10^{-5}$	$6,03 \cdot 10^{-8}$
4498	$-7,71 \cdot 10^{15}$	$-3,42 \cdot 10^{-3}$	$-3,32 \cdot 10^{-8}$	$-3,57 \cdot 10^{-7}$	$8,62 \cdot 10^{-6}$
4501	$3,02 \cdot 10^{18}$	$1,78 \cdot 10^{-2}$	$5,64 \cdot 10^{-8}$	$9,32 \cdot 10^{-7}$	$2,70 \cdot 10^{-6}$
4526	$-1,58 \cdot 10^{17}$	$-3,64 \cdot 10^{-2}$	$-3,74 \cdot 10^{-7}$	$-1,04 \cdot 10^{-5}$	$3,34 \cdot 10^{-7}$
4527	$1,06 \cdot 10^{19}$	$2,36 \cdot 10^{-1}$	$7,49 \cdot 10^{-7}$	$9,36 \cdot 10^{-6}$	$2,80 \cdot 10^{-7}$
4535	$7,91 \cdot 10^{18}$	$4,92 \cdot 10^{-2}$	$1,56 \cdot 10^{-7}$	$2,17 \cdot 10^{-6}$	$8,07 \cdot 10^{-7}$
4548	$-1,70 \cdot 10^{18}$	$-1,91 \cdot 10^{-2}$	$-6,07 \cdot 10^{-8}$	$-8,15 \cdot 10^{-7}$	$2,46 \cdot 10^{-6}$
4559	$2,03 \cdot 10^{19}$	$1,85 \cdot 10^{-1}$	$5,87 \cdot 10^{-7}$	$7,69 \cdot 10^{-6}$	$2,71 \cdot 10^{-7}$
4564	$2,35 \cdot 10^{15}$	$1,06 \cdot 10^{-1}$	$1,09 \cdot 10^{-6}$	$5,22 \cdot 10^{-5}$	$5,42 \cdot 10^{-8}$
4569	$-2,55 \cdot 10^{19}$	$-1,35 \cdot 10^{-1}$	$-4,28 \cdot 10^{-7}$	$-6,00 \cdot 10^{-6}$	$3,41 \cdot 10^{-7}$
4571	$7,16 \cdot 10^{15}$	$2,70 \cdot 10^{-3}$	$2,64 \cdot 10^{-8}$	$6,50 \cdot 10^{-7}$	$3,45 \cdot 10^{-6}$

Table 3.3: Comprehensive summary of chiralities ... (continued)

NGC	κ $[\hat{\kappa}]$	κ_m $[\hat{\kappa}]$	κ_{am} $[\hat{\kappa}]$	κ_{em} $[\hat{\kappa}]$	$\sigma_r(\kappa)$ [1]
4579	$-1,17 \cdot 10^{19}$	$-9,66 \cdot 10^{-2}$	$-3,07 \cdot 10^{-7}$	$-4,83 \cdot 10^{-6}$	$4,12 \cdot 10^{-7}$
4593	$-8,11 \cdot 10^{16}$	$-5,74 \cdot 10^{-2}$	$-5,89 \cdot 10^{-7}$	$-1,81 \cdot 10^{-5}$	$1,05 \cdot 10^{-7}$
4594	$5,17 \cdot 10^{16}$	$3,69 \cdot 10^{-3}$	$3,77 \cdot 10^{-8}$	$5,76 \cdot 10^{-7}$	$3,41 \cdot 10^{-6}$
4621	$-3,88 \cdot 10^{14}$	$-1,38 \cdot 10^{-3}$	$-1,67 \cdot 10^{-8}$	$-7,72 \cdot 10^{-7}$	$2,41 \cdot 10^{-6}$
4636	$-1,77 \cdot 10^{16}$	$-2,87 \cdot 10^{-3}$	$-3,02 \cdot 10^{-8}$	$-7,52 \cdot 10^{-7}$	$1,58 \cdot 10^{-6}$
4651	$9,70 \cdot 10^{16}$	$1,99 \cdot 10^{-2}$	$1,93 \cdot 10^{-7}$	$2,84 \cdot 10^{-6}$	$7,17 \cdot 10^{-7}$
4654	$-2,28 \cdot 10^{18}$	$-1,40 \cdot 10^{-1}$	$-8,73 \cdot 10^{-7}$	$-1,16 \cdot 10^{-5}$	$1,71 \cdot 10^{-7}$
4689	$-2,61 \cdot 10^{17}$	$-1,74 \cdot 10^{-2}$	$-1,08 \cdot 10^{-7}$	$-1,39 \cdot 10^{-6}$	$1,26 \cdot 10^{-6}$
4710	$2,82 \cdot 10^{16}$	$1,62 \cdot 10^{-2}$	$1,66 \cdot 10^{-7}$	$5,13 \cdot 10^{-6}$	$7,58 \cdot 10^{-7}$
4725	$4,07 \cdot 10^{18}$	$1,48 \cdot 10^{-2}$	$4,71 \cdot 10^{-8}$	$7,65 \cdot 10^{-7}$	$2,40 \cdot 10^{-6}$
4731	$3,45 \cdot 10^{17}$	$1,86 \cdot 10^{-1}$	$2,23 \cdot 10^{-6}$	$4,67 \cdot 10^{-5}$	$6,39 \cdot 10^{-8}$
4754	$1,11 \cdot 10^{17}$	$1,87 \cdot 10^{-1}$	$1,92 \cdot 10^{-6}$	$4,56 \cdot 10^{-5}$	$4,88 \cdot 10^{-8}$
4826	$-3,49 \cdot 10^{17}$	$-2,35 \cdot 10^{-2}$	$-2,41 \cdot 10^{-7}$	$-5,30 \cdot 10^{-6}$	$2,86 \cdot 10^{-7}$
4861	$1,61 \cdot 10^{17}$	$1,68 \cdot 10^{-1}$	$1,90 \cdot 10^{-6}$	$4,07 \cdot 10^{-5}$	$8,06 \cdot 10^{-8}$
4866	$7,54 \cdot 10^{14}$	$1,94 \cdot 10^{-2}$	$2,00 \cdot 10^{-7}$	$1,85 \cdot 10^{-5}$	$1,53 \cdot 10^{-7}$
5005	$1,09 \cdot 10^{16}$	$8,84 \cdot 10^{-3}$	$9,23 \cdot 10^{-8}$	$5,00 \cdot 10^{-6}$	$3,83 \cdot 10^{-7}$
5033	$5,68 \cdot 10^{18}$	$8,24 \cdot 10^{-2}$	$2,62 \cdot 10^{-7}$	$2,90 \cdot 10^{-6}$	$6,40 \cdot 10^{-7}$
5055	$-3,14 \cdot 10^{20}$	$-1,84 \cdot 10^{-1}$	$-3,53 \cdot 10^{-7}$	$-5,64 \cdot 10^{-6}$	$3,26 \cdot 10^{-7}$
5204	$2,88 \cdot 10^{17}$	$3,39 \cdot 10^{-1}$	$3,46 \cdot 10^{-6}$	$7,19 \cdot 10^{-5}$	$3,56 \cdot 10^{-8}$
5248	$-2,71 \cdot 10^{17}$	$-4,94 \cdot 10^{-2}$	$-5,08 \cdot 10^{-7}$	$-1,17 \cdot 10^{-5}$	$1,81 \cdot 10^{-7}$
5322	$-1,10 \cdot 10^{15}$	$-3,96 \cdot 10^{-3}$	$-4,67 \cdot 10^{-8}$	$-1,92 \cdot 10^{-6}$	$1,12 \cdot 10^{-6}$
5334	$-2,53 \cdot 10^{16}$	$-2,23 \cdot 10^{-2}$	$-2,27 \cdot 10^{-7}$	$-3,63 \cdot 10^{-6}$	$7,26 \cdot 10^{-7}$
5364	$-3,00 \cdot 10^{17}$	$-2,88 \cdot 10^{-2}$	$-4,13 \cdot 10^{-7}$	$-5,88 \cdot 10^{-6}$	$2,11 \cdot 10^{-7}$
5371	$2,27 \cdot 10^{17}$	$4,78 \cdot 10^{-2}$	$4,92 \cdot 10^{-7}$	$1,10 \cdot 10^{-5}$	$1,54 \cdot 10^{-7}$
5377	$-9,05 \cdot 10^{14}$	$-2,47 \cdot 10^{-3}$	$-2,52 \cdot 10^{-8}$	$-6,22 \cdot 10^{-7}$	$5,23 \cdot 10^{-6}$
5585	$1,02 \cdot 10^{17}$	$1,25 \cdot 10^{-2}$	$1,28 \cdot 10^{-7}$	$2,38 \cdot 10^{-6}$	$6,76 \cdot 10^{-7}$
5669	$6,48 \cdot 10^{16}$	$6,05 \cdot 10^{-2}$	$6,19 \cdot 10^{-7}$	$1,06 \cdot 10^{-5}$	$2,42 \cdot 10^{-7}$
5701	$5,00 \cdot 10^{16}$	$1,16 \cdot 10^{-2}$	$1,19 \cdot 10^{-7}$	$2,63 \cdot 10^{-6}$	$6,02 \cdot 10^{-7}$

Table 3.3: Comprehensive summary of chiralities ... (continued)

NGC	κ $[\hat{\kappa}]$	κ_m $[\hat{\kappa}]$	κ_{am} $[\hat{\kappa}]$	κ_{em} $[\hat{\kappa}]$	$\sigma_r(\kappa)$ [1]
5746	$-4,57 \cdot 10^{18}$	$-1,13 \cdot 10^{0}$	$-1,16 \cdot 10^{-5}$	$-1,69 \cdot 10^{-4}$	$1,96 \cdot 10^{-8}$
5792	$7,00 \cdot 10^{16}$	$6,27 \cdot 10^{-2}$	$6,44 \cdot 10^{-7}$	$1,48 \cdot 10^{-5}$	$2,17 \cdot 10^{-7}$
5813	$1,72 \cdot 10^{16}$	$2,07 \cdot 10^{-2}$	$2,11 \cdot 10^{-7}$	$5,46 \cdot 10^{-6}$	$4,63 \cdot 10^{-7}$
5850	$-9,44 \cdot 10^{16}$	$-7,32 \cdot 10^{-2}$	$-7,47 \cdot 10^{-7}$	$-1,35 \cdot 10^{-5}$	$1,56 \cdot 10^{-7}$
5985	$2,55 \cdot 10^{17}$	$7,58 \cdot 10^{-2}$	$1,51 \cdot 10^{-6}$	$2,43 \cdot 10^{-5}$	$6,26 \cdot 10^{-8}$
6015	$2,11 \cdot 10^{18}$	$5,32 \cdot 10^{-1}$	$5,43 \cdot 10^{-6}$	$9,52 \cdot 10^{-5}$	$2,70 \cdot 10^{-8}$
6118	$6,36 \cdot 10^{16}$	$5,00 \cdot 10^{-2}$	$5,15 \cdot 10^{-7}$	$1,69 \cdot 10^{-5}$	$1,97 \cdot 10^{-7}$
6384	$8,12 \cdot 10^{17}$	$6,07 \cdot 10^{-2}$	$6,24 \cdot 10^{-7}$	$1,06 \cdot 10^{-5}$	$1,25 \cdot 10^{-7}$
6503	$-4,73 \cdot 10^{18}$	$-3,33 \cdot 10^{-1}$	$-3,40 \cdot 10^{-6}$	$-6,26 \cdot 10^{-5}$	$4,03 \cdot 10^{-8}$

Bibliography

L. D. Barron. Can a magnetic field induce absolute asymmetric synthesis? *Science*, 266(5190):1491–1492, 1994.

L. D. Barron. Chirality, magnetism and light. *Nature*, 405:895–896, June 2000.

M. S. Bartlett, editor. *Monte Carlo Methods.* Methuen's monographs on applied probability and statistics. Methuen, Wiley, London, New York, 2 edition, 1964.

I. N. Bronstein, K. A. Semendjajew, G. Musiol, and H. Muehlig. *Taschenbuch der Mathematik.* Harri Deutsch, 2000.

A. B. Buda, T. Auf der Heyde, and K. Mislow. On quantifying chirality. *Angew. Chem. Int. Ed. Engl.*, pages 989–1007, 1992.

A. B. Buda and K. Mislow. A Hausdorff chirality measure. *J. Am. Chem. Soc.*, 114(15):6006–6012, 1992.

J. J. D. de Jong, L. N. Lucas, R. M. Kellogg, J. H. van Esch, and B. L. Feringa. Reversible optical transcription of supramolecular chirality into molecular chirality. *Science*, 304:278–281, April 2004.

G. de Vaucouleurs. In S. Flügge, editor, *Handbuch der Physik*, page 275. Springer-Verlag, Berlin, 1959.

G. de Vaucouleurs. Revised classification of 1500 bright galaxies. *Astrophys. J. Suppl. Ser.*, 8:31, 1963.

G. de Vaucouleurs, A. de Vaucouleurs, H. G. Corwin Jr., R. Buta, G. Paturel, and P. Fouque. *Third Reference Catalogue of Bright Galaxies.* Springer-Verlag, New York, 1991.

Z. Frei, P. Guhathakurta, J. E. Gunn, and J. A. Tyson. A catalog of digital images of 113 nearby galaxies. *Astron. J.*, 111(1):174–181, 1996.

A. B. Harris, R. D. Kamien, and T. C. Lubensky. Molecular chirality and chiral parameters. *Rev. Mod. Phys.*, 71(5):1745–1757, 1999. doi: 10.1103/RevModPhys.71.1745.

L. Hecht and L. D. Barron. Rayleigh and Raman optical activity from chiral surfaces. *Chem. Phys. Lett.*, 225:525–530, 1994. doi: 10.1016/0009-2614(94)87122-1.

I. R. Hooper and J. R. Sambles. Broadband polarization-converting mirror for the visible region of the spectrum. *Opt. Lett.*, 27(24):2152–2154, 2002.

E. Hubble. Extragalactic nebulae. *Astrophys. J.*, 64:321–369, 1926.

E. Hubble. *The Realm of Nebulae.* Yale Univ. Press, New Heaven, 1936.

S. Jain. *Monte Carlo Simulations of disordered systems.* World Scientific Publ., 1992.

W. T. Kelvin. *Baltimore Lectures on Molecular Dynamics and the Wave Theory of Light.* C. J. Clay, London, 1904.

L. D. Landau and E. M. Lifshitz. *Electrodynamics of continuous media*, volume 8 of *Course of theoretical physics.* Pergamon, 2nd edition, 1964.

A. Lauberts and E. A. Valentijn. *The Surface Photometry Catalogue of the ESO-Uppsala Galaxies.* ESO, 1989.

P. Le Guennec. Two dimensional theory of chirality. I. Absolute chirality. *J. Math. Phys.*, 41(9):5954–5985, 2000.

N. Madras, editor. *Lectures on Monte Carlo Methods.* Fields Institute Monographs. American Mathematical Society, 2002.

M. Matsumoto and T. Nishimura. Mersenne twister: A 623-dimensionally equidistributed uniform pseudo-random number generator. *ACM Trans. Model. Comput. Simul.*, 8(1):3–30, 1998. ISSN 1049-3301. doi: 10.1145/272991.272995.

A. Naim, O. Lahav, R. J. Buta, H. G. Corwin Jr., G. de Vaucouleurs, A. Dressler, J. P. Huchra, S. van den Bergh, S. Raychaudhury, L. Sodre Jr., and M. C. Storrie-Lombardi. A comparatative study of morphological classifications of apm galaxies. *Mon. Not. R. Astron. Soc.*, 274(1107-1125), 1995.

M. A. Osipov, B. T. Pickup, M. Fehervari, and D. A. Dunmur. Chirality measure and chiral order parameter for a two-dimensional system. *Mol. Phys.*, 94(2):283–287, 1998. doi: 10.1080/002689798168150.

V. Ostromoukhov. Mathemtical tools for computer-generated ornamental patterns. In *Electronic Publishing, Artistic Imaging and Digital Typography*, Lecture Notes in Computer Science 1375, pages 193–223. Springer Verlag, 1998.

A. Papakostas, A. Potts, D. M. Bagnall, S. L. Prosvirnin, H. J. Coles, and N. I. Zheludev. Optical manifestations of planar chirality. *Phys. Rev. Lett.*, 90(10):107404, 2003. doi: 10.1103/PhysRevLett.90.107404.

J. Pendry. Light runs backward in time. *Physics World*, page 27, June 2000. URL `http://physicsweb.org/article/world/13/6/6`.

J. Pendry. Positively negative. *Nature*, 423:22–23, 2003. doi: 10.1038/423022a.

J. B. Pendry and S. A. Ramakrishna. Focusing light using negative refraction. *J. Phys.: Condens. Matter*, 15:6345–6364, 2003. doi: 10.1088/0953-8984/15/37/004.

M. Petitjean. On the root mean square quantitative chirality and quantitative symmetry measures. *J. Math. Phys.*, 40(9):4587–4595, 1999. doi: 10.1063/1.532988.

M. Petitjean. Chiral mixtures. *J. Math. Phys.*, 43(8):4147–4157, 2002. doi: 10.1063/1.1484559.

M. Petitjean. Chirality and symmetry measures: A transdisciplinary review. *Entropy*, 5(3):271–312, 2003. URL `http://www.mdpi.net/entropy/htm/e5030271.htm`.

A. Potts, D. M. Bagnall, and N. I. Zheludev. A new model of geometric chirality for two-dimensional continuous media and planar meta-materials. *J. Opt. A*, 6:193–203, Feb 2004. doi: 10.1088/1464-4258/6/2/007.

A. Potts, A. Papakostas, N. I. Zheludev, H. J. Coles, R. Greef, and D. M. Bagnall. Planar chiral meta-materials for photonic devices. *J. Mat. Sci.*, 14:393–395, 2003.

V. Prelog. Chirality in chemistry. *Science*, 193:17–24, July 1976.

S. L. Prosvirnin and N. I. Zheludev. Nonreciprocal diffraction of light on a planar chiral structure. arXiv.org, 2003. URL `http://arxiv.org/cond-mat/0309588`.

M. M. I. Saadoun and N. Engheta. Pseudochiral omega-medium and guided-wave structure: Theory and principles. In *Proc. URSI Int. Symp. Electrp-mag. Theory*, pages 17–20, Sydney, August 1992.

A. Sandage. Classification and stellar content of galaxies obtained from direct photography. In A. Sandage, M. Sandage, and J. Kristian, editors, *Galaxies and the Universe*. Univ. Chicago P, 1975.

A. S. Schwanecke, A. Krasavin, D. M. Bagnall, A. Potts, A. V. Zayats, and N. I. Zheludev. Broken time reversal of light interaction with planar chiral nanostructures. *Phys. Rev. Lett.*, 91(24):247404, 2003. doi: 10.1103/PhysRevLett.91.247404.

I. V. Semchenko et al. Reflection and transmission by a uniaxially bi-anistropic slab under normal incidence of plane waves. *J. Phys. D: Appl. Phys.*, 31: 2458–2464, 1998.

A. H. Shivola and I. V. Lindell. Chiral Maxwell-Garnett mixing formula. *Electron. Lett.*, 26(2):118–119, 1990.

A. V. Shubnikov and A. Belov. *Colored symmetry*. Pergamon, 1964.

T. Vallius, K. Jefimovs, J. Turunen, P. Vahimaa, and Y. Svirko. Optical activity in subwavelength-period arrays of chiral metallic particles. *Appl. Phys. Lett.*, 83(2):234–236, 2003. doi: 10.1063/1.1592015.

A. J. Viitanen and P. P. Puska. Reflection from soft and hard surface coated with chiral medium. In *Proc. Bianisotropics 1997*, pages 305–308, 1997.

E. M. Wright and N. I. Zheludev. Broken time reversal and parity symmetries for electromagnetic excitations in planar chiral nanostructures. arXiv.org, 2003. URL `http://arxiv.org/cond-mat/0310023`.

H. Zabrodsky and D. Avnir. Continuous symmetry measures. 4. Chirality. *J. Am. Chem. Soc.*, 117, 1995.

S. Zouhdi, G. E. Couenon, and A. Fourrier-Lamer. Scattering from a peridiodic array of thin planar chiral structures - calculations and measurements. *IEEE Trans. Antennas Propag.*, 47(6):1061–1065, 1999.